Biosurface and Biotribology

WILEY

The Institution of Engineering and Technology

ORIGINAL RESEARCH OPEN ACCESS

Influence of Natural Pathological Alterations on the Mechanical Properties and Microstructure of Human Enamel and Dentine

E. V. Sadyrin[1] | P. E. Antipov[1] | A. P. Evsyukov[1] | A. M. Kolesnikov[2] | A. L. Nikolaev[1]

[1]Don State Technical University, Rostov-on-Don, Russia | [2]Southern Federal University, Rostov-on-Don, Russia

Correspondence: E. V. Sadyrin (esadyrin@donstu.ru)

Received: 12 April 2026 | **Revised:** 6 June 2026 | **Accepted:** 11 June 2026

Keywords: atomic force microscope | biomechanics | dental | enamel | indentation | micromechanical properties | microstructures | morphology | scanning electron microscopy

ABSTRACT

Dental caries represents a significant global health challenge. Accurate quantification of the mechanical properties of dental tissues is essential for understanding disease progression and guiding medical procedures. However, comprehensive comparative analyses across multiple stages of natural caries progression using a unified methodological framework remain limited. This study employs a multimodal approach, integrating several experimental techniques to evaluate the preliminary trends in microstructure and mechanical behaviour of human enamel and dentine affected by white spot lesion in the vicinity of the fissure apex, non-cavitated, and cavitated brown spot lesions. The preliminary results suggest that certain pathological alterations, specifically within the examined brown spot lesions-affected tissues, may display enhanced mechanical properties, which could be attributed to subsurface remineralisation and mineral deposition in sclerotic dentine. In contrast, advanced lesions, particularly those with structural breakdown, appear to exhibit significant reductions in mechanical properties, reflecting extensive demineralisation within the studied specimens. Furthermore, the fissure region was found to be particularly susceptible to mechanical degradation, with localised pathologically altered area seemingly influenced by morphological factors. These initial findings highlight the critical role of microstructural features in modulating the biomechanical response of dental tissues to pathological challenges and provide a basis for broader statistical validation.

1 | Introduction

Human dental hard tissues exhibit a unique hierarchical structure that underpins their exceptional mechanical functionality, enabling resistance to masticatory loads and environmental challenges [1]. Enamel, consisting of highly organised carbonated hydroxyapatite crystallites arranged into prisms [2–4], and dentine, which forms a resilient, less mineralised collagenous matrix secreted by specialised odontoblasts [5–7], constitute a complex biomechanical system. Alterations in their structural integrity due to pathological processes such as caries-associated demineralisation [8–11], erosion [12], hypomineralization [13], wedge-shaped defects [14], or fluorosis [15] can significantly compromise their overall performance [16, 17]. Although dental caries remains the most widespread non-communicable disease globally, heavily impacting public health across all age demographics [18–22], the precise multi-scale mechanics governing its progression across consecutive stages require deeper elucidation.

Accurate quantification of the localised mechanical properties of dental tissues is essential for understanding pathological degradation, designing bioinspired restorative materials, and refining non-invasive clinical interventions [23]. Nanoindentation has emerged as a primary tool for probing submicron-scale mechanical responses [24–26], demonstrating extreme sensitivity to mineral variations and matrix defects [27]. Key milestones in this field include foundational reviews by Angker and Swain [28, 29] and Sadyrin [30]. To date, various researchers have successfully coupled nanoindentation with complementary techniques to explore specific tooth states. For instance, studies have evaluated artificial demineralisation/remineralisation cycles via atomic force microscopy (AFM) [31, 32], bacterial demineralisation in carious dentine using scanning electron microscopy (SEM) [33], and spatial mineral density gradients from the dentine-enamel junction (DEJ) to the pulp via X-ray computed microtomography [34]. Since local geometry and surface artefacts inherently influence nanomechanical measurements [35, 36], multimodal approaches integrating microtomography, optical imaging, or laser speckle analysis are frequently utilised to differentiate early carious lesions from sound tissues [37, 38]. Microbiological and structural evaluations of natural white spot lesions (WSLs) and brown spot lesions (BSLs) have highlighted significant reductions in mechanical properties driven by crystallite-level hierarchical changes, even when the overall macro-architecture appears preserved [39–41]. Furthermore, comparative insights from animal models and natural or artificial dentine lesions indicate complex sub-surface hardness variations and structural alterations extending deeply into intertubular areas [42, 43].

However, despite the extensive use of these methods, a major research gap persists: a comprehensive comparative analysis across multiple consecutive stages of natural caries progression using a unified methodological framework remains limited. Most existing literature focuses on isolated pathological conditions or employs varying experimental parameters, which hinders the direct comparison of tissue behaviour across the continuum of disease progression. To address this gap, the present study combines nanoindentation with AFM, SEM, and optical microscopy to enable a multimodal assessment of the mechanical properties and microstructure in human enamel and dentine subjected to three distinct types of natural pathological alterations: WSL in the vicinity of the fissure apex, non-cavitated BSLs and cavitated BSL.

A key novelty of this work lies in the application of identical instrumentation and testing parameters across all investigated pathological areas within the specimens. This methodological consistency offers a significant clinical and engineering advantage over previous works focussing on a single pathology, allowing for a direct, high-resolution evaluation of how mechanical and microstructural properties manifest through different stages of tissue alteration. Furthermore, special attention is paid to the non-cavitated BSLs. While demineralisation is typically associated with tissue softening, our investigation explores the phenomenon of local increase in mechanical properties observed in this specific stage. We correlate these nanomechanical findings with detailed microstructural analysis, including crystal size measurements and surface topography changes, to elucidate the underlying mechanisms of this hardening effect. By bridging the gap between macroscopic pathology and nanoscale structural changes, this study aims to provide a refined, case-specific understanding of how natural pathological alterations influence the functional competence of dental hard tissues, serving as a preliminary framework for broader multi-scale analyses.

2 | Materials and Methods

Two human molars, extracted for orthodontic reasons at the Maxi-Dent Dental Clinic (Rostov-on-Don, Russia), were selected, and areas of interest corresponding to sound and pathologically altered tissues were identified:

- WSL in the vicinity of the fissure apex: characterised macroscopically by a chalky, opaque appearance with preserved surface continuity; microstructurally, the alteration is confined primarily to the enamel matrix, exhibiting early-stage subsurface demineralisation, partial dissolution of hydroxyapatite crystallites, and a localised porosity increase in intercrystalline and interprism porosity;
- Non-cavitated BSLs: represent a more advanced progression that extend past the DEJ into the underlying dentine; they display a uniform or graded brown pigmentation, yet maintain a macroscopically non-collapsed anatomical contour with a smooth surface;
- Cavitated BSL: presents a clear local macroscopic breakdown of enamel, resulting in a physical loss of surface integrity, which is visually manifested as three distinct structural cavities; this case is further characterised by prominent brown-to-black dentine pigmentation beneath the defect, microstructurally it reveals advanced, uncompensated mineral depletion in enamel with heavily damaged prisms in the vicinity of the fissure apex.

The study protocol was approved by the Local Independent Ethics Committee of Don State Technical University (Decision No. 4, dated 3 July 2025), and written informed consent was obtained from all patients prior to tooth extraction. Immediately after extraction, the teeth were stored in Hanks' Balanced Salt Solution (HBSS) supplemented with thymol granules (Unifarm, Slavyansk-on-Kuban, Russia) for disinfection and prevention of fungal growth. The storage container was kept in a refrigerated pharmaceutical cabinet at 4 ± 2°C. The thymol concentration was maintained at 0.03 g per 30 mL of HBSS.

To facilitate precise sectioning, custom polyethylene terephthalate mounting fixtures were manufactured using a 3D printer. Epoxy-embedded samples were securely positioned within these mounts. Longitudinal sections containing the regions of interest were prepared using a precision saw (Isomet 4000, Buehler, Lake Bluff, IL, USA) equipped with an Al_2O_3-based abrasive disc (Met-Disc-T, MetCata GmbH, Kaufering, Germany). Three parallel sections were obtained from each sample. Section parallelism was maintained using the integrated micrometre adjustment system of the cutting device. The disc rotation speed was set to 4000 rpm, and the feed speed rate was 1.2 mm/min.

The surfaces of the ground sections adjacent to the regions of interest were initially refined using an Al_2O_3-based abrasive disc (P1200 grit) on a Buehler MetaServ 250 grinding/polishing machine (Buehler) under continuous water cooling. Subsequent polishing was performed in multiple stages to achieve a high degree of surface smoothness while preserving the native

microstructure of dental hard tissues and avoiding defects such as microcracks, indentations, or smearing.

The multi-stage polishing protocol employed sequentially finer abrasive suspensions and specialised polishing cloths optimised for brittle, biomineralised materials. In the first stage, rough polishing was conducted using a 15-μm diamond suspension in water applied to the Plan B polishing cloth (Allied High Tech Products Inc., Cerritos, CA, USA)—a dense polyester fabric—effectively removing residual damage from prior cutting and grinding with minimal structural alteration. The second stage utilised a 3-μm diamond suspension on the Vel-Cloth (Allied High Tech Products Inc.), composed of soft synthetic flock, yielding a significantly smoother surface topography. Both stages were carried out with the GreenLube lubricant (Allied High Tech Products Inc.) to minimise thermal and mechanical stress. The final step involved finish polishing with a 0.05-μm aqueous colloidal alumina (Al_2O_3) suspension on the Chem-Pol cloth (Allied High Tech Products Inc.), without additional lubricant. This stage eliminated residual micro-scratches and produced an optically flat, artefact-free surface suitable for high-resolution microscopic and micromechanical characterisation. Between each grinding and polishing stage, samples were ultrasonically cleaned in the Sonorex RK 31 bath (Bandelin, Berlin, Germany) for 5–6 min to ensure complete removal of abrasive residues, wear debris, and contaminants from both the surface and microrelief, thereby preventing cross-contamination and measurement artefacts in subsequent analyses.

Overview images of the prepared samples were acquired using the Zeiss Stereo Discovery V20 stereomicroscope (Carl Zeiss Microscopy GmbH, Oberkochen, Germany) configured according to the Abbe imaging principle [44]. Image acquisition relied on the ZEN 3.0 software (Carl Zeiss Microscopy GmbH) without subsequent focus stacking. Regions of interest for further experimental analyses were identified based on the resulting micrographs. Pigmentation associated with caries progression in enamel in the transmitted light was observed using the Stemi 305 optical stereomicroscope (Carl Zeiss AG, Oberkochen, Germany) with the Greenough illumination and the Axiocam 105 colour video camera (Carl Zeiss AG, Oberkochen, Germany).

The mechanical properties of sound and pathologically altered regions of human dental tissues were evaluated using nanoindentation performed on the NanoTest 600 Platform 3 system (Micro Materials Ltd. Wrexham, UK). All experiments were conducted in the enclosed chamber of the instrument under strict temperature control (27.0 ± 0.1°C). The Berkovich diamond indenter was employed, with loading applied via the pendulum method according to the following protocol: initial preload of 0.05 mN (used as the reference point for constructing the load-displacement curve), followed by loading at the rate of 1.8 mN/s up to a maximum load (P_{max}) of 50 mN. The temperature drift during testing was compensated in real time using the nanoindentation system built-in software. To prevent structural defects due to uncontrolled dehydration, the samples were periodically moistened with distilled water between indentation tests. For each tested region, the contact stiffness (S), reduced Young's modulus (E_r), and indentation hardness (H) were calculated using the Oliver—Pharr method [45, 46]. Additionally, creep behaviour during the hold segment at the peak load was recorded to enable deeper viscoelastic analysis. The geometric correction factor $\beta = 1.034$ was applied in the reduced elastic modulus calculation, as recommended in [47]. Calculation algorithm and the detailed workflow are given in Appendix A. Optical microscopy of the tissue regions surrounding the residual imprints was performed using the integrated optical system of the nanoindentation instrument, equipped with an Olympus U-TLU objective lens and an Olympus TH4-200 illumination source (Olympus Corp., Tokyo, Japan).To ensure the accuracy of the contact area function calibration, standard fused silica (fused quartz) and sapphire reference samples were used prior to the experiments.

The surface topography of the regions under study was acquired using the NT-206 AFM (Microtest Machines, Gomel, Belarus). Samples were secured to a removable magnetic stage using adhesive carbon tape, identical to that employed in SEM sample preparation. Prior to each imaging session, the AFM was calibrated using a TGZ1 silicon calibration grating [48]. This procedure included adjustment of the scan frame's dimensional scale. Both the calibration grating and the samples were imaged using a two-pass scanning mode. Scan parameters were optimised for each region: the scan delay was increased as needed to enhance image quality, while the height and width settings were adjusted to define the field of view. All scans were performed with a resolution of 256 × 256 pixels, resulting in a lateral sampling pitch of 45.7 nm. Imaging was carried out using new NSC11 probes (MikroMasch, Innovative Solutions Bulgaria Ltd., Sofia, Bulgaria), featuring a tip radius of curvature of approximately 10.0 nm and a nominal cantilever spring constant of 48 N/m. To rigorously monitor the tip condition, the probe radius was evaluated using SEM. The Gwyddion 2.69 software (Czech Metrology Institute, Brno, Czech Republic) was used for image processing. The Gaussian filter with a 1-pixel standard deviation was applied.

The surfaces of the dental tissues were visualised using the Crossbeam 340 SEM (Carl Zeiss Microscopy GmbH, Oberkochen, Germany). Prior to analysis, the sections underwent sequential chemical cleaning and dehydration: immersion in 3.25% NaClO solution for 3 min, followed by graded dehydration in isopropyl alcohol (25%, 50%, and 70% v/v for 5 min each; 80%, 90%, and 95% v/v for 15 min each), and final dehydration in 100% isopropyl alcohol (v/v) for 30 min with two solution changes. Sample 2, Section 2 was additionally immersed in 100% isopropyl alcohol (v/v). Thereafter, a 19.0–20.1-nm-thick carbon layer was deposited on the section surfaces using a Quorum Q150TES Plus turbomolecular-pumped, combined sputter coater and carbon evaporation system (Quorum Technologies Ltd. Laughton, UK) operated in a pulsed current mode under a vacuum of 1×10^{-4} mbar. The SEM imaging of the tooth tissues was performed using the Everhart-Thornley secondary electron detector at an accelerating voltage of 2 kV and an aperture size of 30 μm.

3 | Results and Discussion

Optical images of the sample sections, with regions of interest highlighted, are shown in Figure 1. Sets of force-displacement curves were obtained for the dental tissues, and data from unsuccessful indentation tests were excluded (Figures 2–4). The curves were analysed, and indentation parameters were processed using the nanoindentation system software. The resulting

mechanical properties are summarised in Tables 1–6. Analysis of the experimental results showed that the typical mechanical characteristics of sound enamel and dentine were obtained for both samples and all sections [28–30].

Although data were acquired across multiple AFM channels, only the most informative images from the Topography channel were selected for analysis. This channel provides the highest-resolution representation of surface topography and enables the construction of accurate height-difference (profile) maps.

For Sample 1, Section 1 (Figures 5–7), an area of reduced mechanical characteristics was found, which can be attributed to enamel demineralisation in the immediate vicinity of the fissure

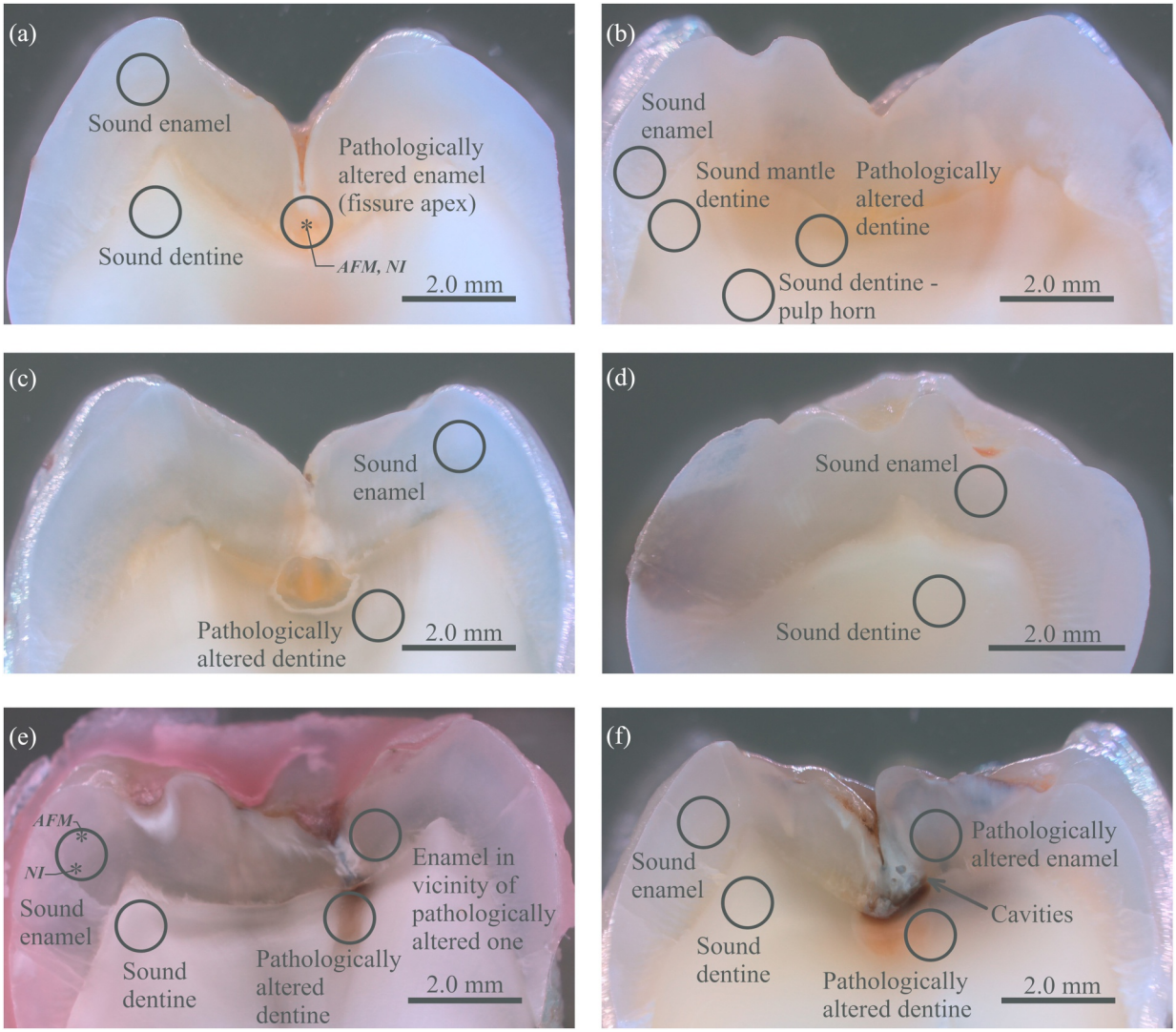

FIGURE 1 | Samples under research: (a) Sample 1, Section 1, (b) Sample 1, Section 2, (c) Sample 1, Section 3, (d)—Sample 2, Section 1, (e) Sample 2, Section 2, (f) Sample 2, Section 3. The notations *AFM, NI indicate the refined measurement zones for AFM and nanoindentation experiments.

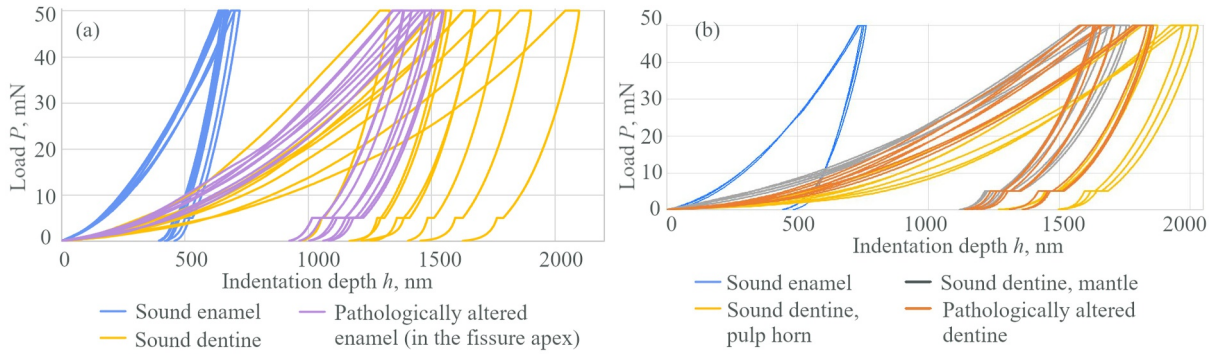

FIGURE 2 | Force-displacement curves for the Sample 1. (a) Section 1, (b) Section 2.

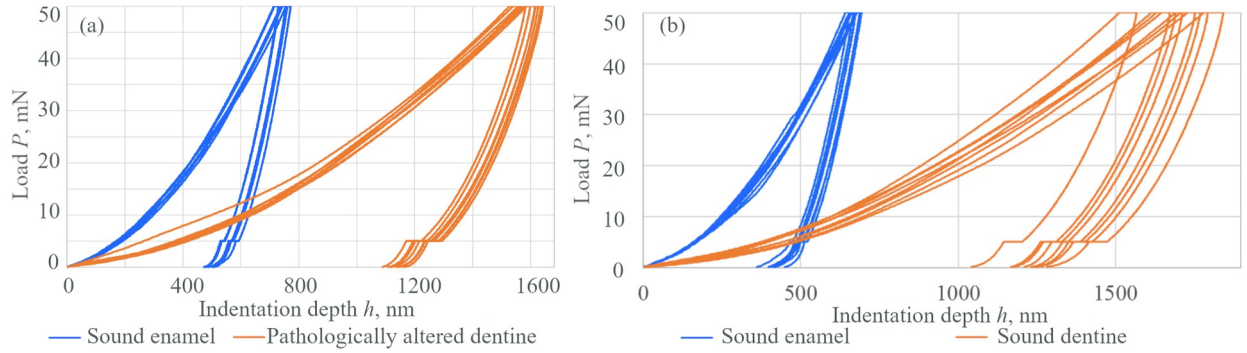

FIGURE 3 | Force-displacement curves for the (a) Sample 1, Section 3, (b) Sample 2 Section 1.

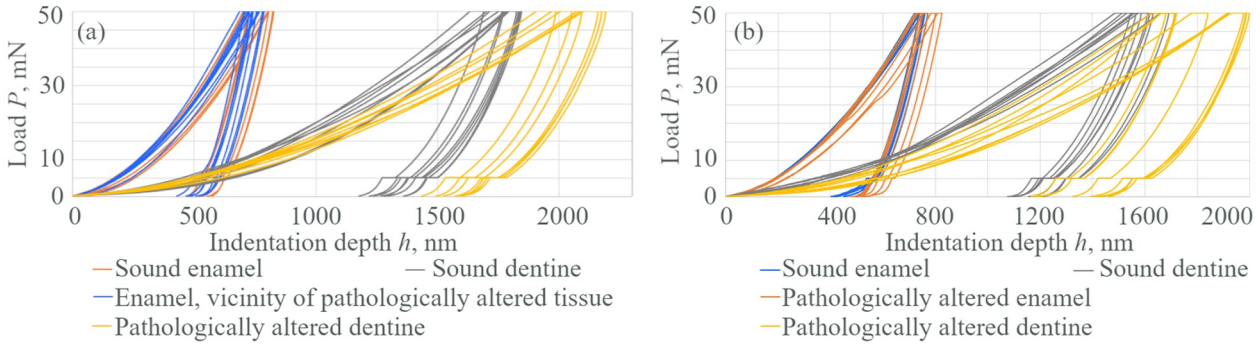

FIGURE 4 | Force–displacement curves for the (a) Sample 2, Section 2, (b) Sample 2, Section 3.

TABLE 1 | The values of tooth tissue contact characteristics and mechanical properties.

Area under study	Max. depth h_{max}, nm	Contact depth h_c, nm	Hardness H, GPa	Reduced young's modulus E_r, GPa	Stiffness S, mN/nm	Creep C_{IT}, nm
Sound enamel	678.6 ± 24.6	572.7 ± 24.4	4.91 ± 0.35	95.12 ± 4.59	0.35 ± 0.011	14.8 ± 1.6
Pathologically altered enamel[a]	1699.6 ± 232.5	1557.9 ± 227.7	1.00 ± 0.22	32.11 ± 4.34	2.65 ± 0.012	43.3 ± 4.5
Sound dentine	1470.3 ± 66.5	1297.0 ± 66.4	1.27 ± 0.10	29.54 ± 1.34	0.22 ± 0.005	43.1 ± 2.4

Note: Sample 1, Section 1.
[a]Demineralised enamel in the fissure apex.

TABLE 2 | The values of tooth tissue contact characteristics and mechanical properties.

Region of interest	Max. depth h_{max}, nm	Contact depth h_c, nm	Hardness H, GPa	Reduced young's modulus E_r, GPa	Stiffness S, mN/nm	Creep C_{IT}, nm
Sound enamel	754.2 ± 7.7	647.26 ± 4.60	3.96 ± 0.05	84.74 ± 3.75	0.35 ± 0.014	18.5 ± 1.6
Sound dentine—mantle	1704.8 ± 56.4	1502.8 ± 47.0	1.02 ± 0.05	22.75 ± 1.70	0.19 ± 0.010	61.5 ± 3.3
Sound dentine—pulp horn	1931. 3 ± 80.8	1748.9 ± 84.4	0.83 ± 0.05	22.67 ± 0.69	0.21 ± 0.007	52.0 ± 4.0
Pathologically altered dentine[a]	1736.7 ± 97.2	1557.9 ± 99.0	0.97 ± 0.1	25.03 ± 1.02	0.21 ± 0.005	49.7 ± 2.2

Note: Sample 1, Section 2.
[a]Light brown uniform pigmentation.

apex (the Young's modulus, hardness and stiffness are 2.96, 4.91 and 7.57 times lower compared to the sound enamel). From a mechanical perspective, the complex topography of the occlusal surface plays an important role in the localised stress-strain state in the enamel. Classic dental biomechanics literature utilising mathematical modelling and experimental methods has robustly demonstrated that deep occlusal grooves induce severe stress concentration under functional masticatory loading that may lead to formation of localised zones with reduced enamel mineralisation [49–51]. This geometric vulnerability is well-documented

TABLE 3 | The values of tooth tissue contact characteristics and mechanical properties.

Region of interest	Max. depth h_{max}, nm	Contact depth h_c, nm	Hardness H, GPa	Reduced young's modulus E_r, GPa	Stiffness S, mN/nm	Creep C_{IT}, nm
Sound enamel[a]	751.5 ± 15.3	646.2 ± 16.6	3.98 ± 0.18	86.07 ± 2.02	0.36 ± 0.009	15.2 ± 0.7
Pathologically altered dentine[b]	1617.9 ± 19.9	1434.8 ± 21.7	1.08 ± 0.02	25.87 ± 0.42	0.21 ± 0.004	51.9 ± 2.5

Note: Sample 1, Section 3.
[a]Cusp.
[b]Light brown uniform pigmentation.

TABLE 4 | The values of tooth tissue contact characteristics and mechanical properties.

Region of interest	Max. depth h_{max}, nm	Contact depth h_c, nm	Hardness H, GPa	Reduced young's modulus E_r, GPa	Stiffness S, mN/nm	Creep C_{IT}, nm
Sound enamel	677.7 ± 14.1	574.3 ± 14.2	3.74 ± 0.53	83.26 ± 5.69	0.19 ± 0.002	12.8 ± 1.0
Sound dentine	1725.1 ± 84.6	1531.1 ± 85.0	0.99 ± 0.08	23.33 ± 0.94	0.36 ± 0.009	57.5 ± 3.5

Note: Sample 2, Section 1.

TABLE 5 | The values of tooth tissue contact characteristics and mechanical properties.

Region of interest	Max. depth h_{max}, nm	Contact depth h_c, nm	Hardness H, GPa	Reduced young's modulus E_r, GPa	Stiffness S, mN/nm	Creep C_{IT}, nm
Sound enamel	779.6 ± 53.4	674.2 ± 53.6	3.74 ± 0.52	83.26 ± 5.69	0.36 ± 0.002	17.5 ± 1.0
Enamel in the vicinity of the pathologically altered tissue[a]	747.8 ± 29.1	646.2 ± 28.8	3.99 ± 0.30	89.48 ± 5.00	0.37 ± 0.014	15.5 ± 0.9
Sound dentine	1800.4 ± 55.0	1611.7 ± 55.6	0.92 ± 0.05	23.15 ± 1.11	0.20 ± 0.009	53.5 ± 6.4
Pathologically altered dentine[b]	2118.4 ± 77.3	1909.5 ± 74.2	0.74 ± 0.04	18.74 ± 0.75	0.18 ± 0.003	79.9 ± 2.8

Note: Sample 2, Section 2.
[a]In the vicinity of dark brown localised spot.
[b]Dark brown localised spot.

TABLE 6 | The values of tooth tissue contact characteristics and mechanical properties.

Region of interest	Max. depth h_{max}, nm	Contact depth h_c, nm	Hardness H, GPa	Reduced young's modulus E_r, GPa	Stiffness S, mN/nm	Creep C_{IT}, nm
Sound enamel	753.2 ± 11.42	649.3 ± 13.9	3.94 ± 0.14	86.90 ± 1.51	0.36 ± 0.011	16.6 ± 0.9
Pathologically altered enamel[a]	768.8 ± 32.8	665.0 ± 33.5	3.80 ± 0.31	85.40 ± 3.38	0.36 ± 0.071	15.7 ± 0.7
Sound dentine	1620.0 ± 58.7	1437.1 ± 57.0	1.08 ± 0.06	25.90 ± 1.13	0.21 ± 0.005	54.2 ± 2.9
Pathologically altered dentine[b]	1862.7 ± 140.5	1675.1 ± 137.8	0.88 ± 0.1	22.8 ± 1.86	0.20 ± 0.009	57.8 ± 6.0

Note: Sample 2, Section 3.
[a]Light brown uniform pigmentation.
[b]In the vicinity of brown-to-black localised spot.

across both clinical and computational studies. For instance, Lagouvardos et al. [52] conducted an in vivo clinical evaluation of molar and premolar anatomy across two hundred patients, identifying cusp geometry—specifically deep central fossae—as a primary factor predisposing teeth to structural failure. To elucidate the underlying mechanics, Spears and Crompton [53] successfully employed finite element analysis (FEA) to map stress gradients at the contacting interfaces of occlusal cusps. Similarly, an FEA approach was utilised by Magne and Belser [54] to investigate the horizontal components of compressive forces that drive cusp bending and wedging, which consequently induce significant tensile stresses within the fossa region. Furthermore, the mechanisms of interaction between food and the occlusal surface of the tooth were studied by Bourdiol and Mioche [55], while Salis et al. [56] experimentally validated these stress pathways by evaluating the fracture patterns of a series of intact premolars subjected to uniform loading on the lingual slopes of buccal cusps. Extant scientific literature suggest that direct occlusal loading generates intense excessive localised stress around the loading area and further affect crack formation [57, 58]. In clinical practice [59, 60],

such fractures were observed to propagate either longitudinally along the fissure into the underlying tooth tissue or completely sever one of the cusps.

Furthermore, the progression of demineralisation in the regions in the vicinity of the fissures may be exacerbated by cariogenic bacteria that preferentially accumulate at fissure apices [61].

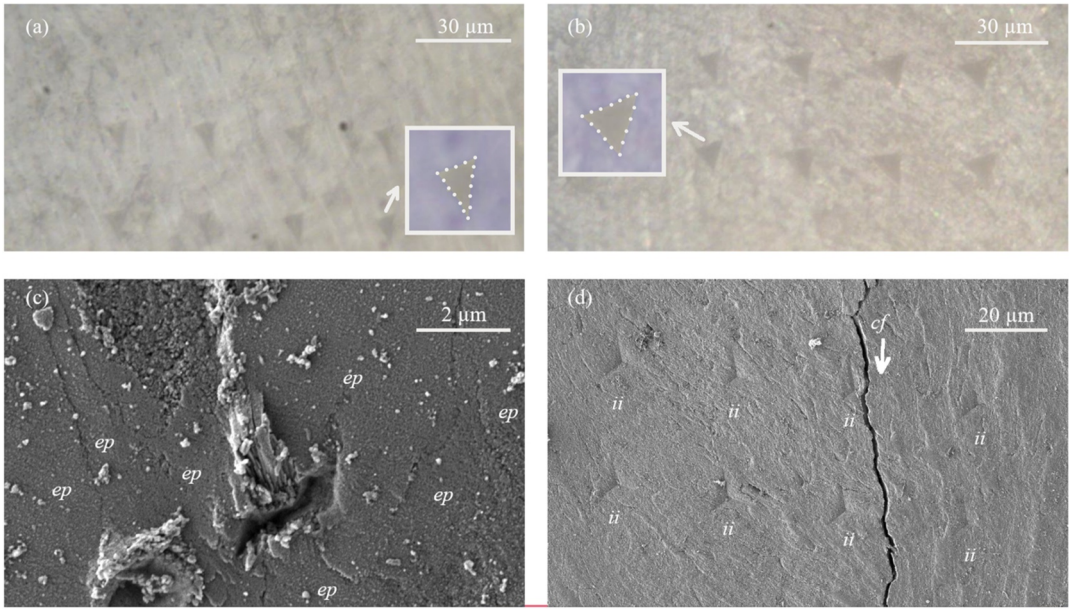

FIGURE 5 | Optical and SEM micrographs of Sample 1, Section 1: (a) sound enamel (optical image); (b) pathologically altered enamel at the fissure apex (optical image); (c) sound enamel (SEM image); (d) pathologically altered enamel at the fissure apex (SEM image); *ep*—enamel prisms, *ii*—indentation imprints, *cf*—crack extending from the fissure. Insets show indentations at approximately 1.9-fold magnification relative to the main images.

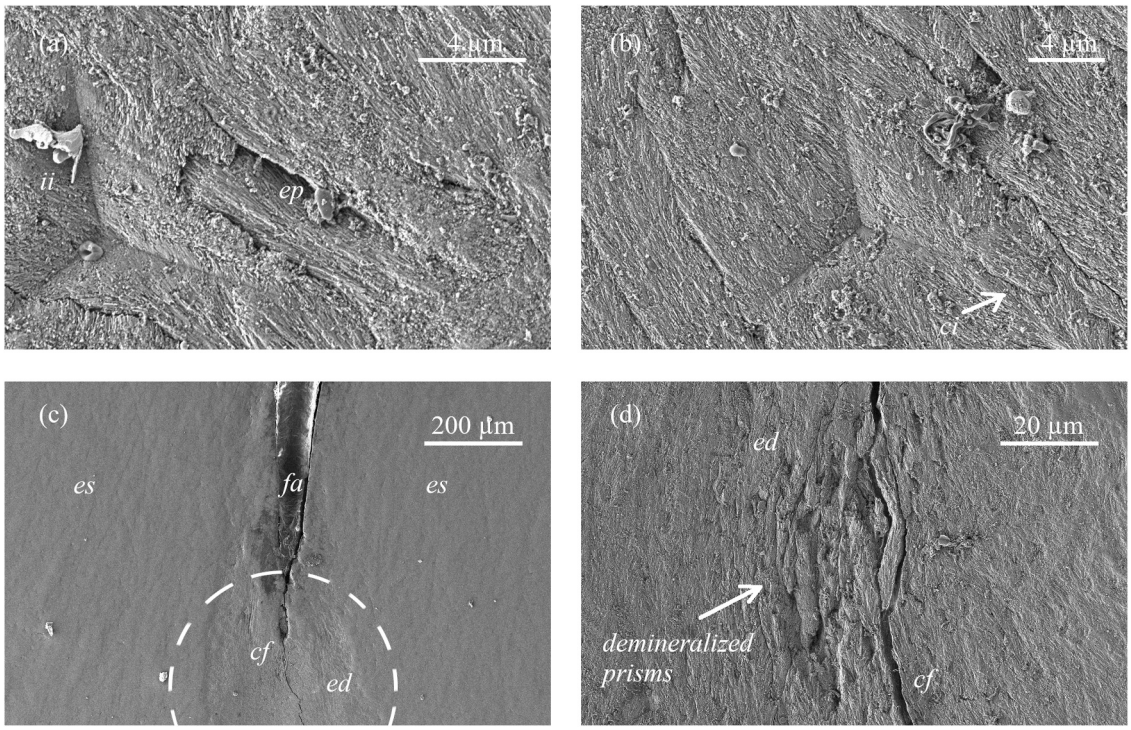

FIGURE 6 | SEM-obtained microstructural features of Sample 1, Section 1: (a) sound enamel—enamel prism covered by smear layer, (b) sound enamel—crack in the indentation imprint tip (marked with the arrow), (c) demineralised area beneath the fissure apex, (d) demineralised prisms; *ep*—enamel prisms, *ii*—indentation imprints, *fa*—fissure apex, *cf*—crack extending from the fissure, *es*—enamel sound, *ed*—enamel demineralised. Note the localised overcharging effect at the fissure apex in (c), which is a characteristic SEM imaging artefact presumably caused by the steep local geometry and the high concentration of organic matter in the deep recess; this effect is strictly confined to the apex boundary and does not affect the interpretation of the surrounding enamel microstructure.

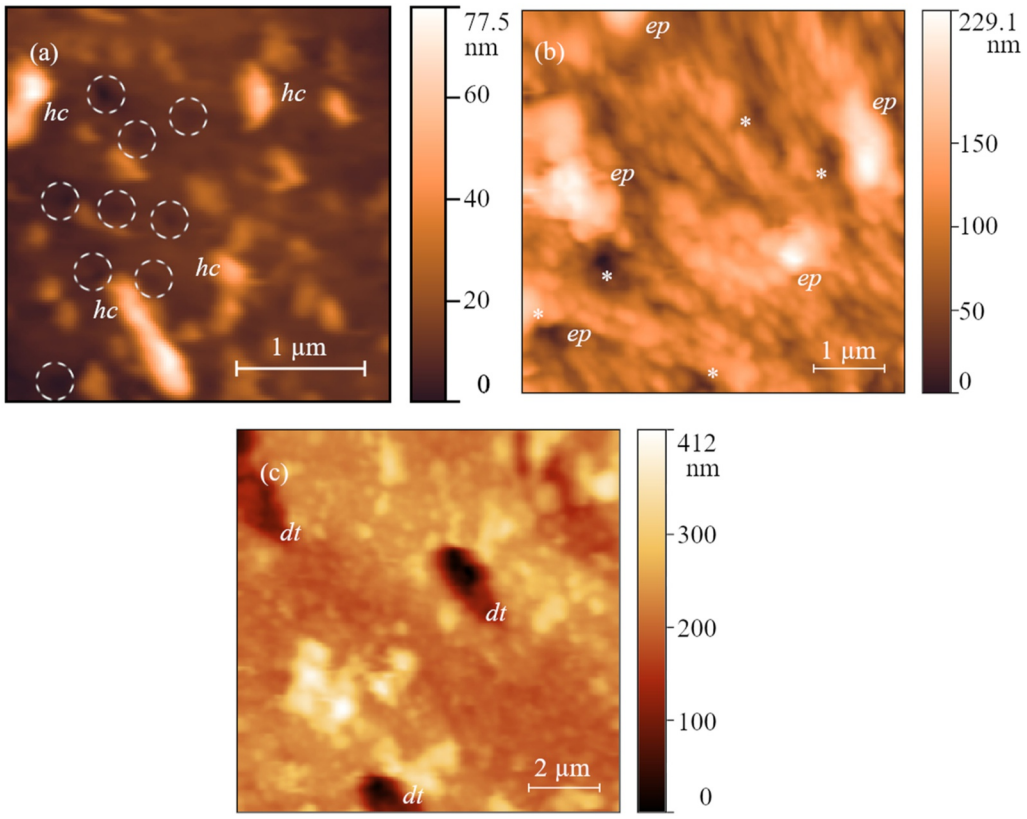

FIGURE 7 | AFM surface images of Sample 1, Section 1: (a) sound enamel; (b) pathologically altered enamel; (c) sound dentine; *ep*—enamel prisms, *hc*—crystallites/arrays of hydroxyapatite crystallites; *dt*—dentinal tubules. Dotted circles mark the depressions in the enamel surface. The sites of the absent crystallites are marked with *.

Other enamel breakdown mechanisms were also recognised, often linked to intrinsic structural heterogeneities, microstructural peculiarities, or locally insufficient enamel thickness—all of which predispose the tissue to subsequent demineralisation [62, 63], see less structured surface of the pathologically altered tissue in Figure 5b (some of the crystallites were missing from the structure, see Figure 7b) compared to the sound counterpart in Figures 5a and 7a.

A similar phenomenon has been observed in WSL enamel [64], albeit to a lesser degree. Moreover, the impaired load-resistance mechanism of the tissue is reflected in the shape of the deformation curves (Figure 2a, purple curve), where not only the indentation depth under load changed, but also the slopes of the loading and unloading branches.

Comparison of sound and pathologically altered enamel SEM images (Sample 1, Section 1) reveals distinct structural features. In both cases, enamel prism boundaries are discernible across most areas. Sound enamel is covered by a relatively uniform smear layer, whereas pathologically altered enamel at the fissure apex exhibits a more porous surface morphology with protruding hydroxyapatite crystals. This appearance likely results from the partial dissolution of hydroxyapatite crystallites during pathological demineralisation, which makes them more susceptible to fracture during sample preparation. Consequently, many prism outlines are obscured by a layer of displaced crystallites (Figure 6a). While most indentations lack corner cracks, isolated microcracks (Figure 6b) are observed and are likely associated with dehydration-induced embrittlement of the residual organic matrix (note that there were no major cracks during nanoindentation when the sample was hydrated, Figure 5b).

Such indentations act as stress concentration sites, promoting crack initiation—a mechanism that likely also contributed to the crack observed at the fissure apex (Figure 6c,d), which extends down to the indentation area (see Figure 5d). Note the more pronounced manifestation of the crack in the SEM micrograph compared to the optical microscopy image, which is presumably attributed to localised matrix shrinkage and stress relaxation under high-vacuum desiccation.

Figures 8–10 represent the microstructural features of Sample 1, Section 2, Figures 11 and 12—Sample 1, Section 3, Figures 13 and 14—Sample 2, Section 1. For the pathologically altered dentine of Sample 1, Section 2, as well as for the enamel adjacent to pathologically altered tissue in Sample 2, Section 2 (Figures 15b and 16b), a slight increase in mechanical properties was observed compared to the sound tissues. In the dentine, the reduced Young's modulus increased by 10.02%, hardness remained nearly unchanged, and stiffness rose by 10.53% relative to the sound mantle dentine (Figure 9b). Compared to the sound dentine near the pulp horn (Figures 8b and 10c), the same altered region exhibited increases of 10.41% in reduced Young's modulus and 16.87% in hardness, while stiffness values remained comparable. Figure 9 reveals distinct dentine microstructural features. Firstly, the tubules of the sound

dentine (Figure 9a) are open, and secondly, the inter-tubular space between the peritubular mineralised cuffs around the tubules appears to be denser in the pathologically altered tissue (Figure 9b). It should be noted that the 'indentation load-indentation depth' curves for such pathologically altered dentine exhibit two distinct deformation behaviours: one more resistant to load and the other less so (Figure 2b, orange curve), indicating that the tooth tissue is non-uniform in its mechanical properties (which is unsurprising, as not all tubules exhibit exactly the same microstructure as shown in Figure 9b throughout the region of interest).

In the enamel of the Sample 2, Section 2, the tissue close to the BSL zone showed increases of 7.47%, 6.68%, and 2.78% in reduced Young's modulus, hardness, and stiffness, respectively, relative to the adjacent sound enamel (Figures 15a and 16a). Figure 15f shows a dense cluster of hydroxyapatite crystallites in the pathologically altered tissue. The indentation load-depth curves for this enamel are characteristic of sound tissue, as evidenced by the nearly identical loading and unloading branches in Figure 4a (blue and orange curves).

A comparable behaviour was noted in the enamel of Sample 2, Section 3, where the sound tissue (Figures 17 and 18)—pathologically altered tissue pair exhibited close values of mechanical properties rather than the expected contrast. The indentation load-depth curves for these tissues are similar as well (Figure 4b, blue and orange curves). This phenomenon may be attributed to increased mineralisation (Figure 19) of the pathologically altered tissue—a compensatory response of the tooth biomechanical system to caries, as described by Shahmoradi and Swain [65].

BSLs are clinically regarded as arrested and partially remineralised carious lesions [66], although the relationship between their characteristic colouration and remineralisation status remains a subject of debate. Several studies have reported

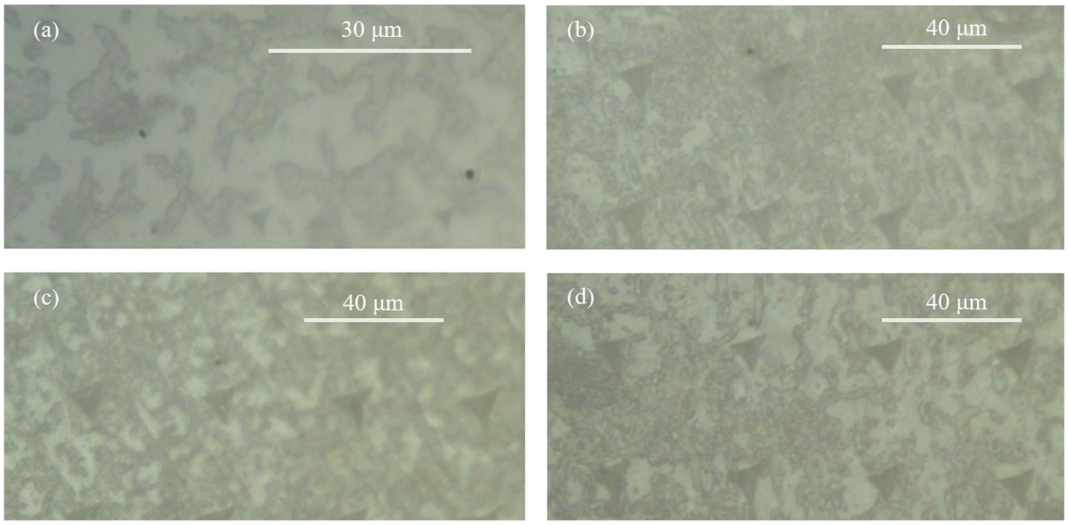

FIGURE 8 | Indentation impressions on the regions of under study of Sample 1, Section 2: (a) sound enamel, (b) sound dentine—pulp horn, (c) sound mantle dentine, (d) pathologically altered dentine. Note the darker background contrast of the sound enamel (a) compared to the wiped overview images; this variation is an optical effect caused by the continuous presence of a fluid layer maintained during the in situ nanoindentation experiments to prevent tissue dehydration.

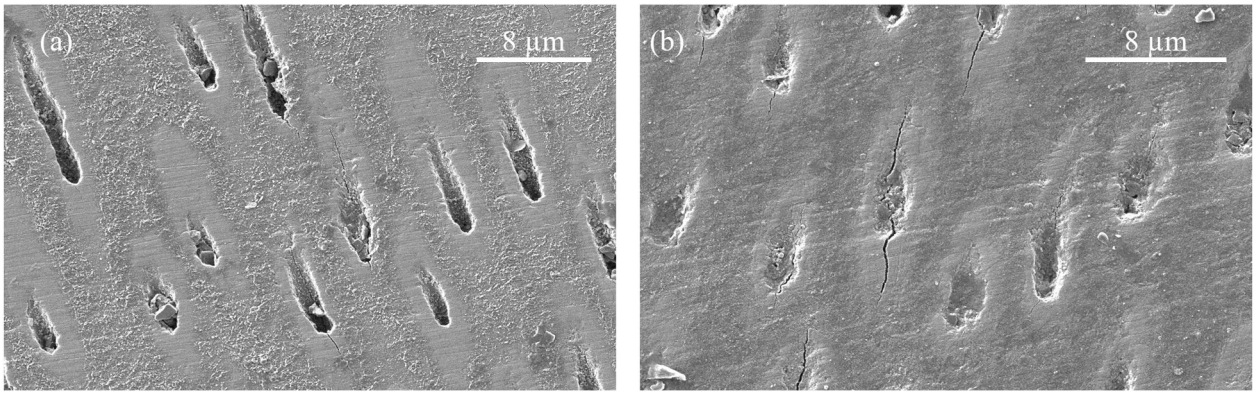

FIGURE 9 | Dentinal tubules in Sample 1, Section 2: (a) sound dentine—pulp horn, (b) pathologically altered dentine.

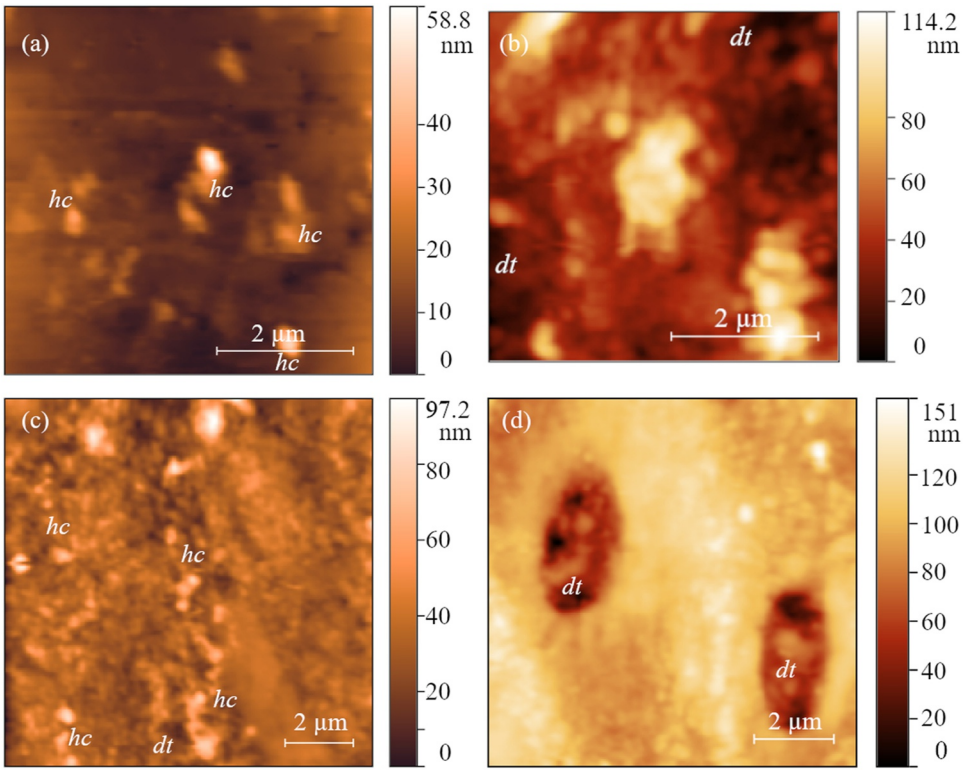

FIGURE 10 | AFM surface images of Sample 1, Section 2: (a) sound enamel; (b) sound dentine—mantle; (c) sound dentine in the vicinity of the pulp horn; (d) pathologically altered dentine; *hc*—crystallites/arrays of hydroxyapatite crystallites; *dt*—dentinal tubules.

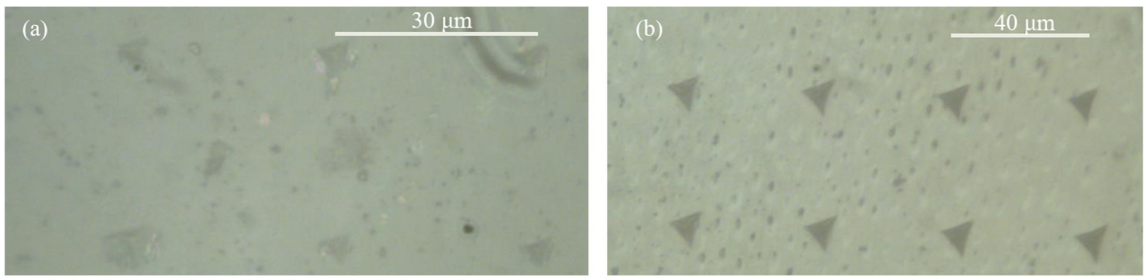

FIGURE 11 | Indentation impressions on the regions under study of Sample 1, Section 3: (a) sound enamel, (b) pathologically altered dentine.

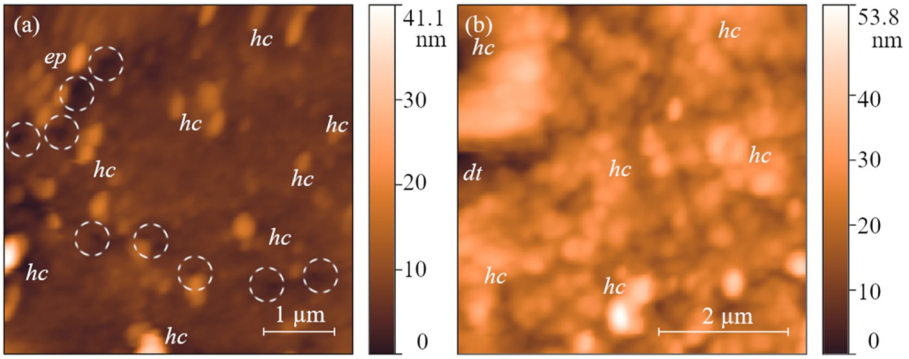

FIGURE 12 | AFM surface images of Sample 1, Section 3: (a) sound enamel; (b) pathologically altered dentine; *ep*—enamel prisms, *hc*—crystallites/arrays of hydroxyapatite crystallites; *dt*—dentinal tubules. Dotted circles mark the depressions in the enamel surface.

increased mineral content and enhanced mechanical resistance of the BSL outer layer [67, 68], suggesting a surface remineralisation degree. Nevertheless, the internal microstructure and spatial distribution of minerals within BSLs have not yet been investigated extensively, particularly using high-resolution nanoindentation techniques.

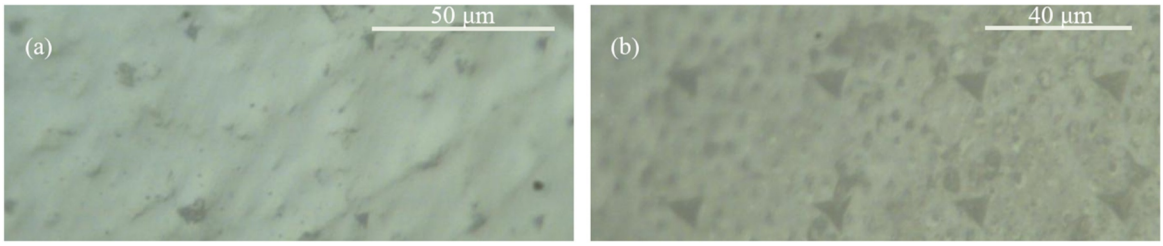

FIGURE 13 | Indentation impressions on the regions under study of Sample 2, Section 1: (a) sound enamel, (b) sound dentine.

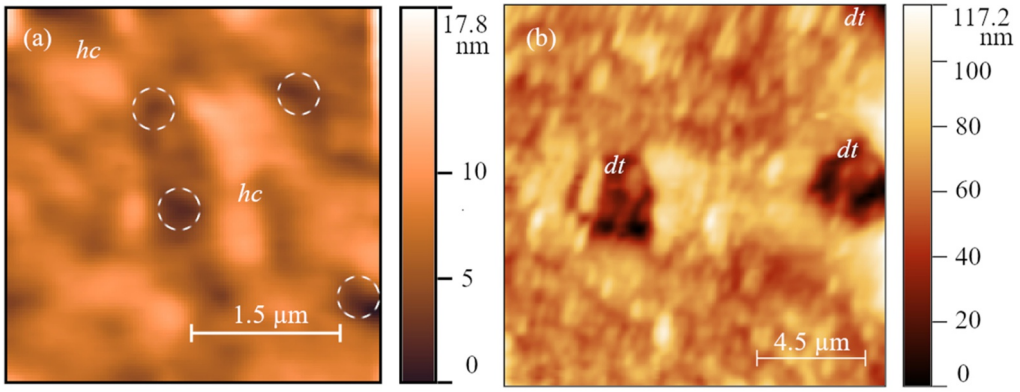

FIGURE 14 | AFM surface images of Sample 2, Section 1: (a) sound enamel, (b) sound dentine; *hc*—crystallites/arrays of hydroxyapatite crystallites; *dt*—dentinal tubules. Dotted circles mark the depressions in the enamel surface.

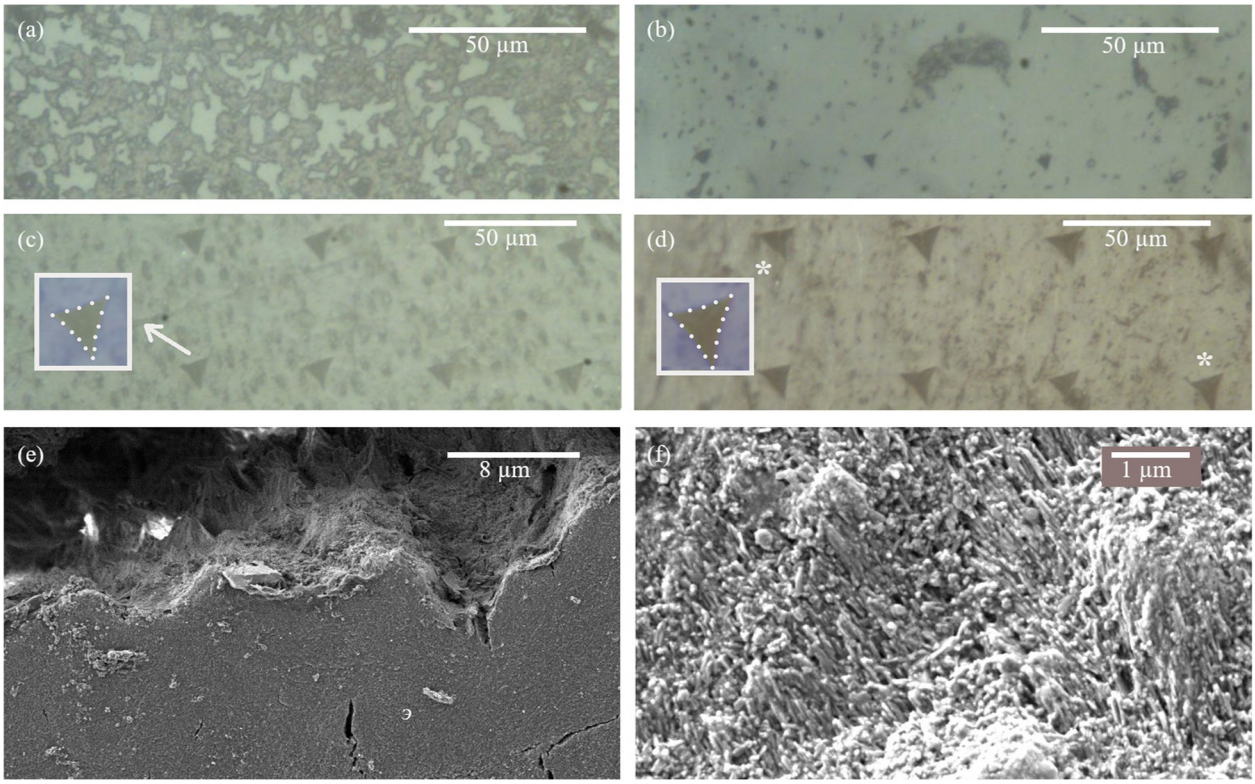

FIGURE 15 | Optical and SEM micrographs of Sample 2, Section 2: (a) indentation imprints in sound enamel (optical image), (b) indentation imprints in enamel in the pathologically altered tissue vicinity (optical image), (c) indentation imprints in sound dentine (optical image), (d) indentation imprints in pathologically altered dentine (optical image), (e) pathologically altered dentine, (f) cluster of hydroxyapatite crystallites in pathologically altered enamel. Insets show the imprints at approximately 1.8-fold magnification relative to the main images. Note the darker background contrast of the sound enamel (a) compared to the wiped overview images; this variation is an optical effect caused by the continuous presence of a fluid layer maintained during the in situ nanoindentation experiments to prevent tissue dehydration.

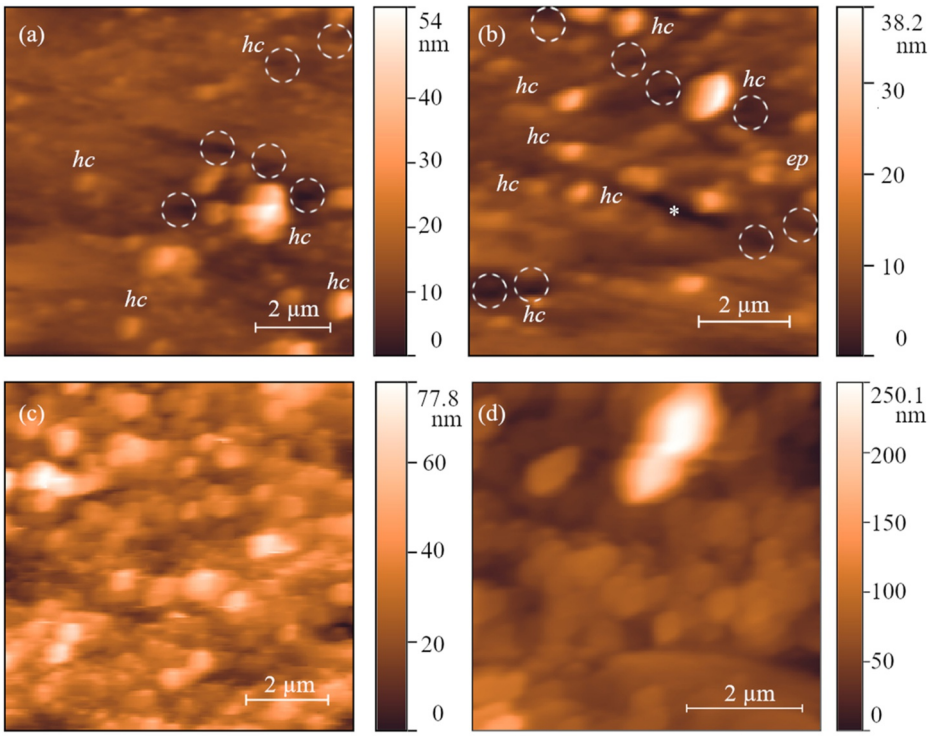

FIGURE 16 | AFM surface images of Sample 2, Section 2: (a) sound enamel, (b) enamel in the vicinity of pathologically altered tissue, (c) sound dentine, (d) pathologically altered dentine; *hc*—crystallites/arrays of hydroxyapatite crystallites, *ep*—enamel prisms. The symbol * indicates a depression in the enamel, presumably obtained during the formation of the section.

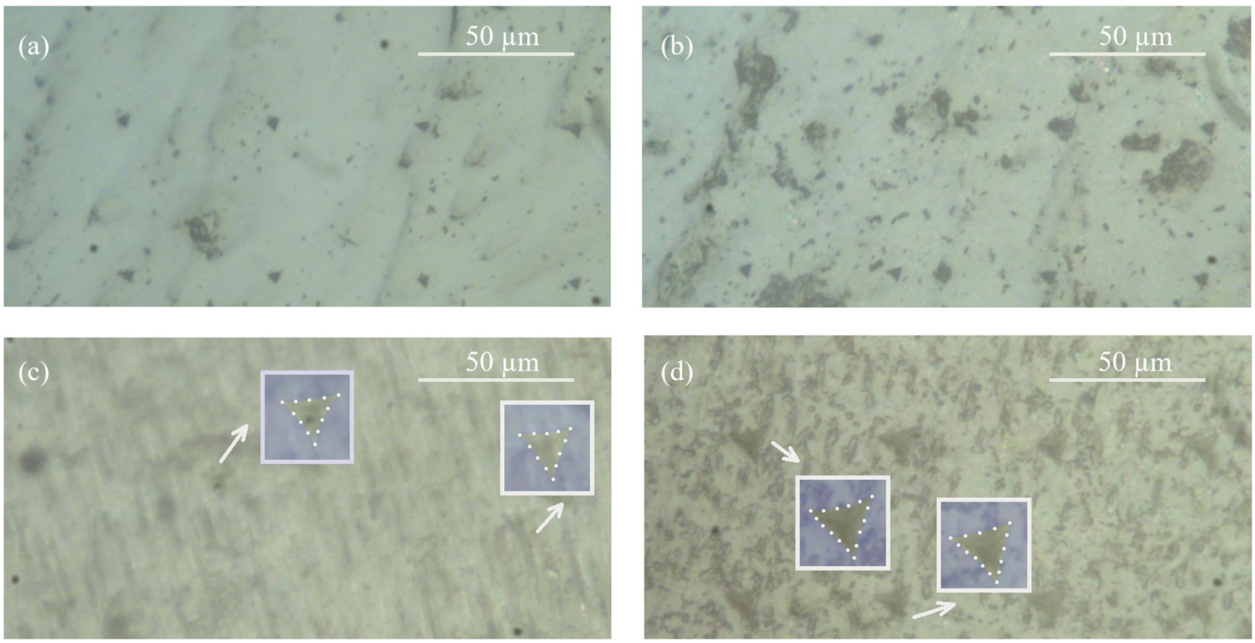

FIGURE 17 | Indentation impressions on the regions under study of Sample 2, Section 3: (a) sound enamel, (b) pathologically altered enamel, (c) sound dentine, (d) pathologically altered dentine. Insets show the imprints at approximately 1.3-fold (c) and 1.4-fold (d) -fold magnification relative to the main images.

This finding aligns with microstructural observations: the pathologically altered enamel retains an acquired smear layer comparable to that of the sound enamel (Figures 18a and 20b), despite the proximity of the BSL with cavity formation (Figure 20c; see also Figure 1f for the macro visualisation of the areas mentioned). Notably, enamel within the carious cavity exhibits a collapsed microstructure with loss of prism definition, giving the appearance of a fused or amorphous surface layer (Figure 20d). Figure 1e,f and 21a,b show enamel discolouration adjacent to the BSLs, which appears less pronounced in Sample 2, Section 2 than in Sample 2, Section 3. During the transmitted light microscopy examination of the zone adjacent to the DEJ, distinct linear

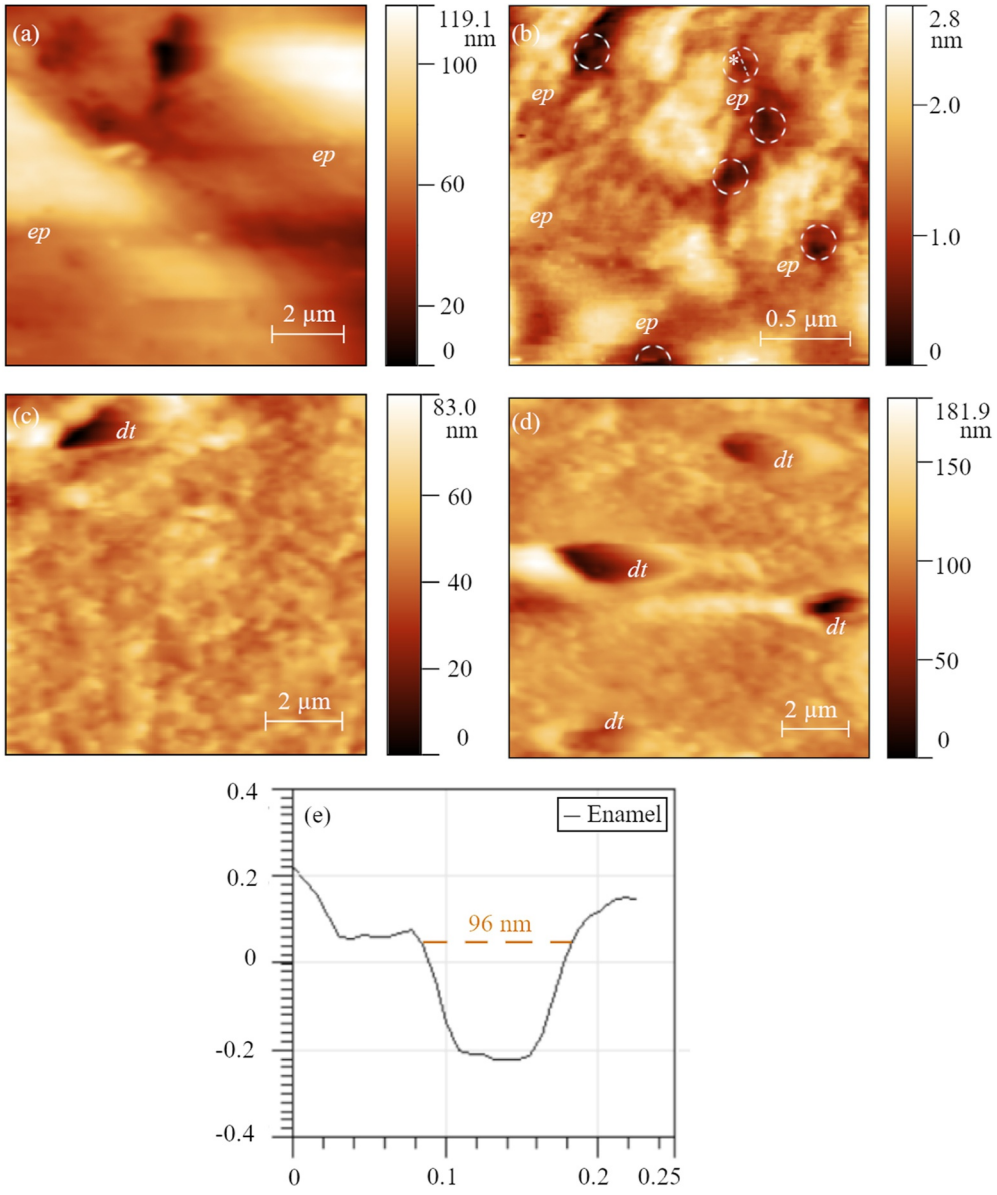

FIGURE 18 | AFM surface images of Sample 2, Section 3: (a) sound enamel; (b) pathologically altered enamel; (c) sound dentine; (d) pathologically altered dentine; *ep*—enamel prisms, *dt*—dentinal tubules. Dashed circles indicate depressions in the enamel sections. The profile of one of them, marked with *, was measured (e).

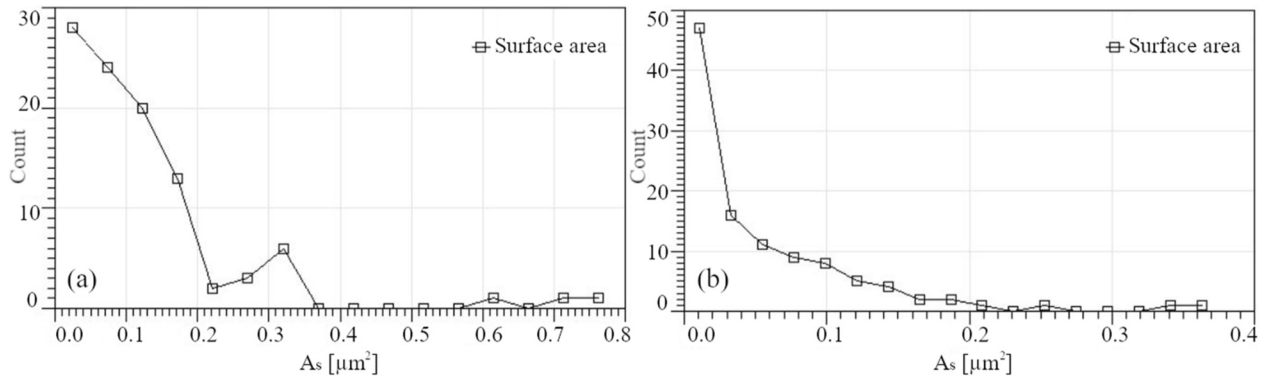

FIGURE 19 | AFM derived surface area of the crystallites for the Sample 2, Section 2: (a) sound enamel; (b) enamel in the vicinity of pathologically altered tissue.

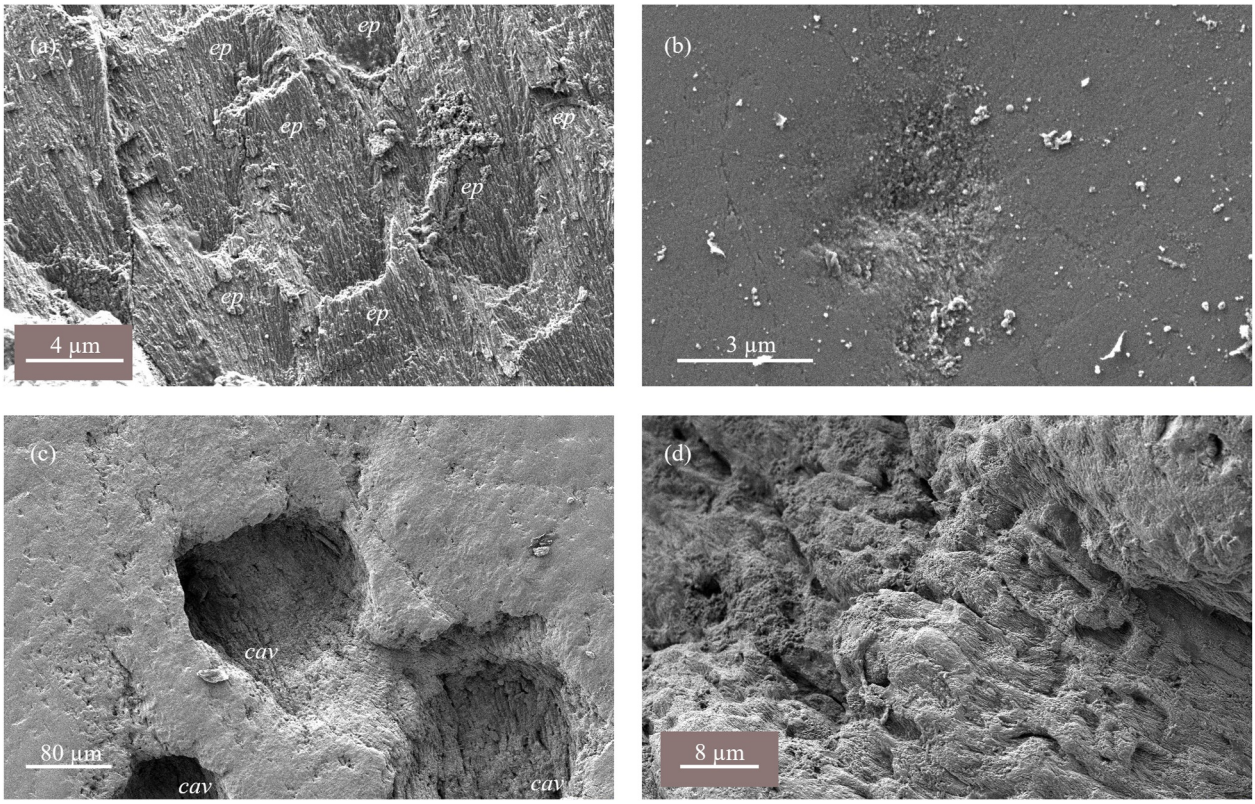

FIGURE 20 | SEM enamel micrographs of Sample 2, Section 3: (a) sound enamel; (b) pathologically altered enamel (above the BSL carious cavities); (c) cavities; (d) assembly of prisms with pathological alterations; *ep*—enamel prism, *cav*—carious cavity.

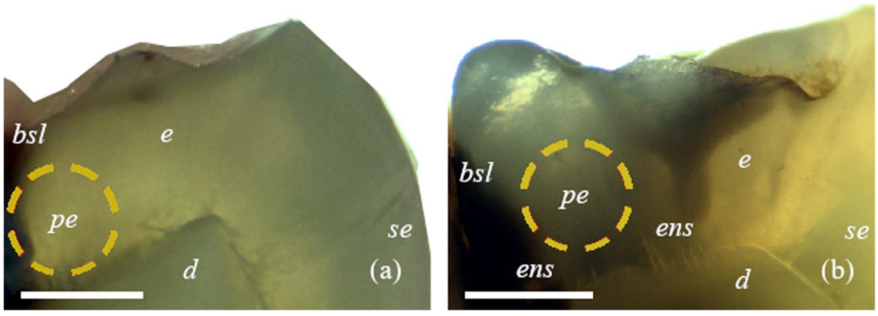

FIGURE 21 | Enamel discolouration in the vicinity of the BSLs obtained—optical microscopy (transmitted light, white balance corrected), Sample 2: (a) Section 2; (b) Section 3; *e*—enamel, *d*—dentine, *bsl*—brown spot lesion, *pe*—pigmented pathologically altered enamel in the vicinity of the BSL spot, *se*—sound enamel, *ens*—enamel spindles. Scale bar: 2. 0 mm.

features extending from the dentine towards the early enamel layers were captured (Figure 21b). Based on their characteristic morphology, location, and orientation, these microstructural features may be preliminarily identified as enamel spindles [69]—anatomical structures representing the trapped terminal branches of dentinal tubules. In the transmission imaging mode, these features exhibit a noticeably high brightness. However, further systematic investigations of a larger series of DEJs remain essential for a definitive anatomical verification of these structures and their precise role in caries progression.

The proposed mechanism suggests that, in response to acidogenic bacteria and the acids they produce during the caries progression from enamel into dentine, minerals are actively transported towards the demineralised site in enamel. This process potentially results in the formation of new crystallites and the growth of pre-existing ones, matching the preferred orientation of sound enamel. Notably, this structure lacks directional growth and forms a layer over the entire surface of the enamel sample, with some small crystallites underneath [70].

The phenomenon of smaller crystallites' growth may be visualised using the diagrams of the grain surface area A_s from the pair 'sound enamel—enamel in the vicinity of the pathologically altered tissue' (Figure 19) via the watershed segmentation algorithm (note the less pronounced smear layer for the demineralised tissue, Figure 15b). Lower crystallite packing potentially allows easier diffusion of acids and protons into the tissue and mineral ions out [71]. The absence of distinct boundaries within the examined areas suggests that localised dissolution might have

resulted in the loss of crystallite structure and fusion, diminishing preferred orientation. In dentine, this process often manifests as tubular sclerosis, characterised by the progressive mineralisation of tubule lumens, which can ultimately lead to their complete occlusion [72] (note the 'closed' tubules in Figure 9b vs. either open ones or those filled with the preparation-induced smear layer debris, Figures 7c and 9a). In addition to hydroxyapatite crystallites, large crystals of magnesium-substituted β-tricalcium phosphate (β-TCP, whitlockite [73]) are known to form in the carious lesion during dentine sclerosis [74]. However, in the examined more advanced carious lesions—typically accompanied by dark brown pigmentation—the reduction in the dentine mechanical properties was observed (Figure 4a,b).

Specifically, in Sample 2, Section 3, demineralised dentine showed decreases of 11.97%, 18.52%, and 4.76% in the reduced Young's modulus, hardness, and stiffness, respectively, compared to the sound dentine. In Sample 2, Section 2, similar comparisons revealed reductions of 19.05%, 19.57%, and 10.0% in reduced Young's modulus, hardness, and stiffness, respectively. Note the less steep loading branches and greater indentation depths observed for pathologically altered dentine in both Sections 2 and 3 (Figure 4a,b, yellow curves). In Appendix B the representative micrographs of the AFM probe tip as well as the DEJ of this sample is given in Figures B1 and B2.

From a biomechanical perspective, the primary objective of dentine remineralisation is to restore the functional competence and structural integrity of the affected tissue. Structurally, collagen fibrils in dentine serve as a scaffold for mineral crystallites, thus providing support for surrounding enamel. This mineralised architecture is critical for preserving tooth function, as it actively prevents the propagation of cracks from the brittle enamel through the DEJ into the underlying dentine, thereby mitigating the risk of crown fractures [75]. However, upon penetrating the dentine, the rapid progression of natural carious lesions establishes distinct pathological zones characterised by sharp gradients in mineral content, microstructural damage, and compromised nanomechanical properties. Existing literature demonstrates that mineral regrowth within these heterogeneous zones remains viable [76–79]. This subsurface remineralisation can proceed either through the spontaneous incorporation of calcium, phosphate, and fluoride ions from oral fluids onto remnant hydroxyapatite crystallites (with fluoride modulating the kinetics of the naturally occurring dissolution and re-precipitation processes at the tissue-fluid interface [80]) or via the external therapeutic delivery of these mineral ions.

Crucially, the occurrence of subsurface remineralisation within advanced enamel-dentine lesions extending beyond the DEJ such as those evaluated in this study (Figures 1f, 17d and 20b) depends heavily on two critical limiting factors. First, the local concentration of mineral ions at the precipitation site must exceed the supersaturation threshold for hydroxyapatite. This requires that not all calcium and phosphate ions entering through the lesion pores have already been precipitated in the layers closer to the surface. Second, the site of precipitation requires nuclei for precipitation, considering that substantially larger degrees of supersaturation are needed for de novo precipitation of apatite or precipitation onto remaining organic matrix than on fragments of enamel or dentine crystallites [81]. Moreover, newly precipitated mineral phases can act as continuous templates for further nucleation of salivary calcium and phosphate ions, facilitating sustained remineralisation over time. Crucially, even if the remineralised matrix does not fully recover the nanomechanical properties characteristic of sound dentine, it often demonstrates significantly enhanced resistance to subsequent acid attacks [82].

In addition to matrix remineralisation, tubular sclerosis (occlusion) plays a critical role in altering the localised mechanical response of carious dentine. From a micromechanical perspective, sound dentine behaves as a permeable cellular solid, free water in dentine is a dynamic phase, and its movement through the porosities and tubules in dentine may influence the response of bulk dentine structure during mechanical functions [83]. Sclerosis of tubules via the formation of minerals within the intratubular spaces represents a natural defence mechanism against caries attack, thereby occluding the tubules and preventing acids and cariogenic bacteria from advancing deeper into the tooth. This mechanism may be mediated by the carious-induced stimulated odontoblastic processes with a source of mineral being the pulpal blood supply. A second mechanism which results in a partial mineralisation of the tubule lumens may be due to the re-precipitation of the dissolved apatite from low supersaturated aqueous phase [6]. These processes could potentially modulate the boundary conditions during localised mechanical testing. Specifically, as nanoindentation arrays traverse these sclerotic zones, the reduction or absence of empty tubular spaces appears to mitigate the tissue's susceptibility to localised micro-deformation.

An important feature observed during the nanoindentation is the material displacement around the residual imprint: in the stiffer biological tissues, the material exhibits sink-in behaviour (inward displacement along the imprint perimeter), and this effect diminishes with decreasing tissue stiffness [84]. Notably, pile-up (outward material displacement), commonly observed in soft materials such as Au films [85], was not detected in the tissues with minor pathological alterations (magnified insets in Figure 16b,c) as well as in those with pronounced changes (increased insets in Figures 5a,b and 15b,c). For the examined specimens, this observation tentatively suggests that such tissues appear to retain a certain load-bearing capacity, which may reflect the preservation of a relatively high strain-hardening coefficient [86].

In nanoindentation experiments, creep [87] refers to the progressive deformation of a material under a constant maximum load. The increased porosity in the pathologically altered enamel and dentine regions is likely a key factor underlying this rheological behaviour. AFM topographical maps and SEM micrographs clearly reveal that demineralisation induces a distinct microstructural transition. Thus, in carious enamel areas, this is demonstrated by the partial dissolution of crystallites (Figures 6c,d and 7b). In the pathologically altered dentine the structure may become more open compared to the sound counterpart because of the loss of mineral especially within the collagen-rich intertubular region. From a material science perspective, this qualitative loss of structural density directly governs the altered structure–property relationship.

Consequently, the quantitative escalation in creep compliance serves as a direct mechanical fingerprint of the micro- and nanoscale architectural disruption visually demonstrated by our multimodal imaging. Figure 18e presents a cross-section of a single depression in enamel with a diameter of less than 100 nm. These depressions may correspond to nanopores inherent to the enamel microstructure [2, 88, 89].

The integrated findings from the aforementioned quantitative mechanical and microstructural analyses provide preliminary evidence supporting the occurrence of subsurface remineralisation in the naturally arrested BSLs within the examined specimens. This reinforces the view of BSLs as valuable natural models for investigating the caries remineralisation dynamics. However, a deeper understanding of the biological and physicochemical mechanisms driving this process along with the environmental conditions that promote or hinder it remains essential. Such knowledge could potentially guide the future design of biomimetic remineralisation therapies' design and non-invasive clinical strategies for caries management. Moreover, exploring remineralisation under extreme conditions such as elevated temperatures [90] or microgravity [91] (e.g., in space environments) could offer unique insights into the resilience and fundamental limits of these innate repair mechanisms.

Several limitations of the present study should be acknowledged, suggesting directions for future work. A primary limitation of this investigation is the small biological sample size, as the mechanical and structural data were obtained from only two extracted human molars. This restriction may limit the immediate generalisability of the absolute values across broader patient demographics, where factors like age, diet, and systemic health vary. However, it should be noted that a high density of nanoindentation testing locations and a comprehensive selection of specific areas of interest were utilised to rigorously characterise the properties within these specimens. Future studies incorporating a larger and more diverse cohort of teeth are required to validate the statistical variance of these pathological trends on a population scale. Secondly, the X-ray microtomography [92, 93] is required to map mineral density variations throughout caries progression in both enamel and dentine and to correlate these changes with mechanical properties. Such analysis would enable investigation of larger tissue volumes under near-physiological, liquid-filled conditions (ideally prior to the nanoindentation and SEM analyses) thereby avoiding artefacts introduced by section preparation and dehydration. Thirdly, the mechanisms underlying newly precipitated hydroxyapatite crystallites' formation require further investigation using the X-ray diffraction techniques [70, 94]. Also, energy-dispersive X-ray spectroscopy [95, 96] should also be applied to assess the stoichiometry and detect ionic substitutions within the crystal lattice. Furthermore, incorporating additional complementary analytical techniques, such as Raman spectroscopy, presents a highly promising avenue for future investigations [97]. Correlating localised nanomechanical data with site-specific Raman compositional mapping would allow for a precise evaluation of mineral-to-organic ratios, crystallinity changes, and chemical alterations within natural carious lesions. Such multi-scale, correlative approaches are essential to establish direct links between structural degradation, chemical transformations, and the overall biomechanical response of hard dental tissues.

This study highlights the potential importance of extending biomechanical and bioengineering investigations to various pathological alteration forms in dental tissues, such as fissure caries and cavitated carious lesions. While early-stage lesions offer insights into incipient demineralisation and natural remineralisation processes, advanced pathologies involving fissure demineralisation or cavity formation present distinct mechanical challenges. These include localised stress concentrations, compromised structural integrity, altered load-bearing capacity, and complex interactions between residual hard tissue and microbial biofilms. The detailed biomechanical characterisation of such lesions through the nanoindentation, microstructural imaging, and computational modelling [98–102] can provide critical data for understanding lesion progression, predicting fracture risk, and informing the design of minimally invasive restorative strategies. Moreover, integrating bioengineering principles into the analysis of cavitated and fissure caries may potentially pave the way for novel diagnostic tools, biomimetic materials, and patient-specific therapeutic approaches that account not only for biological but also mechanical aspects of dental tissue degradation and repair.

4 | Conclusion

This study provides preliminary insights into the biomechanical characterisation of sound and pathologically altered human enamel and dentine using nanoindentation in conjunction with the microscopic techniques. The results suggest that certain carious alterations, particularly enamel and dentine affected by the BSLs, can potentially exhibit increased nanomechanical properties which may be attributed to subsurface remineralisation and mineral deposition in sclerotic dentine. In contrast, advanced carious lesions, especially those accompanied by dark pigmentation and structural breakdown, appear to show substantial decreases in the reduced Young's modulus, hardness, and stiffness, reflecting extensive demineralisation and loss of the tissue integrity within the examined specimens.

Notably, the fissure region acting as natural stress concentrator appeared to be particularly susceptible to mechanical degradation, with localised WSL areas of reduced mineralisation seemingly influenced by the morphological factors such as fissure geometry and surface quality. These findings highlight the critical role of microstructural features in modulating the biomechanical response of dental tissues to pathological challenges. From a clinical perspective, these nanomechanical markers offer valuable diagnostic and therapeutic insights. Tracking localised variations in hardness and elastic modulus can support the development of next-generation, non-invasive diagnostic tools, such as chairside micro-mechanical probes or advanced optical monitoring systems [103], capable of detecting early subsurface degradation before macroscopic cavitation occurs. Moreover, naturally arrested lesions emerge as excellent biological models for understanding endogenous remineralisation processes offering potential inspiration for biomimetic therapeutic strategies. Demonstrating that these areas can naturally regain the mechanical properties of the tissues provides a strong biomechanical rationale for minimally invasive management strategies, encouraging a clinical shift from cavity preparation towards biomimetic therapeutic protocols aimed at preserving and therapeutically reinforcing structurally compromised dental tissues.

While these preliminary observations are limited by the small biological cohort, it remains essential to elucidate the dynamic interplay between microbial activity, host-derived mineral transport, and mechanical adaptation in carious tissues, including those subjected to extreme environmental conditions. Such research could potentially facilitate the development of non-invasive diagnostics, preventive protocols, and bioinspired restorative materials that preserve both the biological vitality and mechanical resilience of the dentition.

Acknowledgements

The study was funded by the Grant 25-29-00829 issued by the Russian Science Foundation, https://rscf.ru/project/25-29-00829/. The sample preparation, nanoindentation and scanning electron microscopy were performed on the equipment of the Resource Center for Collective Use of the Scientific and Educational Center 'Materials' of Don State Technical University (RCCU DSTU). The authors gratefully acknowledge Prof. M.V. Swain (University of Sydney, Sydney, Australia) for his insightful guidance in data interpretation, Dr. L.I. Krenev (Don State Technical University, Rostov-on-Don, Russia) for his assistance with sample preparation, and Prof. S.Yu. Maksyukov (Maxi-Dent Dental Clinic, Rostov-on-Don, Russia) for providing the biological samples.

Funding

This work was funded by Russian Science Foundation (Grant 25-29-00829).

Ethics Statement

The study protocol was approved by the Local Independent Ethics Committee of Don State Technical University (Decision No. 4, dated 3 July 2025).

Consent

Written informed consent was obtained from two patients of the Maxi-Dent Dental Clinic (Rostov-on-Don, Russia) prior to tooth extraction on 23 April 2025, and 20 January 2025.

Conflicts of Interest

The authors declare no conflicts of interest.

Data Availability Statement

Data available on request from the authors.

References

1. Z. Zhou, P. Constantino, M. Hoffman, et al., "Dental Biotrobiology: Final Thoughts and Future Directions," *Biosurface and Biotribology* 3, no. 4 (2017): 119–123, https://doi.org/10.1016/j.bsbt.2017.11.001.

2. E. D. Yilmaz, G. A. Schneider, and M. V. Swain, "Influence of Structural Hierarchy on the Fracture Behaviour of Tooth Enamel," *Philosophical Transactions of the Royal Society A: Mathematical, Physical & Engineering Sciences* 373, no. 2038 (2015): 20140130, https://doi.org/10.1098/rsta.2014.0130.

3. T. Kono, T. Sakae, H. Nakada, T. Kaneda, and H. Okada, "Confusion Between Carbonate Apatite and Biological Apatite (Carbonated Hydroxyapatite) in Bone and Teeth," *Minerals* 12, no. 2 (2022): 170, https://doi.org/10.3390/min12020170.

4. L. H. He and M. V. Swain, "Enamel—A Functionally Graded Natural Coating," *Journal of Dentistry* 37, no. 8 (2009): 596–603, https://doi.org/10.1016/j.jdent.2009.03.019.

5. S. N. White, M. L. Paine, W. Luo, et al., "The Dentino-Enamel Junction Is a Broad Transitional Zone Uniting Dissimilar Bioceramic Composites," *Journal of the American Ceramic Society* 83, no. 1 (2000): 238–240, https://doi.org/10.1111/j.1151-2916.2000.tb01181.x.

6. A. V. Zavgorodniy, R. Rohanizadeh, and M. V. Swain, "Ultrastructure of Dentine Carious Lesions," *Archives of Oral Biology* 53, no. 2 (2008): 124–132, https://doi.org/10.1016/j.archoralbio.2007.08.007.

7. K. M. Galler, M. Weber, Y. Korkmaz, M. Widbiller, and M. Feuerer, "Inflammatory Response Mechanisms of the Dentine–Pulp Complex and the Periapical Tissues," *International Journal of Molecular Sciences* 22, no. 3 (2021): 1480, https://doi.org/10.3390/ijms22031480.

8. A. Erickson, E. Rond, and S. L. Cravens, "Investigating the Demineralisation of Hydroxyapatite by Kombucha and Hard Seltzer Using Atomic Force Microscopy," *Biosurface and Biotribology* 11, no. 1 (2025): e12088, https://doi.org/10.1049/bsb2.12088.

9. J. S. Zuluaga-Morales, M. V. Bolaños-Carmona, C. C. Cifuentes-Jiménez, and P. Álvarez-Lloret, "Chemical. Microstructural and Morphological Characterisation of Dentine Caries Simulation by pH-Cycling," *Minerals* 12, no. 1 (2021): 5, https://doi.org/10.3390/min12010005.

10. K. Yoshihara, N. Nagaoka, A. Nakamura, et al., "Three-Dimensional Observation and Analysis of Remineralization in Dentinal Caries Lesions," *Scientific Reports* 10, no. 1 (2020): 4387, https://doi.org/10.1038/s41598-020-61111-1.

11. D. J. White, "The Application of in Vitro Models to Research on Demineralization and Remineralization of the Teeth," *Advances in Dental Research* 9, no. 3 (1995): 175–193, https://doi.org/10.1177/08959374950090030101.

12. J. Zheng, F. Xiao, L. Zheng, L. M. Qian, and Z. R. Zhou, "Erosion Behaviors of Human Tooth Enamel at Different Depth," *Tribology International* 43, no. 7 (2010): 1262–1267, https://doi.org/10.1016/j.triboint.2009.12.008.

13. K. Elhennawy, D. J. Manton, F. Crombie, et al., "Structural. Mechanical and Chemical Evaluation of Molar-Incisor Hypomineralization-Affected Enamel: A Systematic Review," *Archives of Oral Biology* 83 (2017): 272–281, https://doi.org/10.1016/j.archoralbio.2017.08.008.

14. L. Sakhabutdinova, A. A. Kamenskikh, A. G. Kuchumov, Y. Nosov, and I. Baradina, "Numerical Study of the Mechanical Behaviour of Wedge-Shaped Defect Filling Materials," *Materials* 15, no. 20 (2022): 7387, https://doi.org/10.3390/ma15207387.

15. T. Aoba and O. Fejerskov, "Dental Fluorosis: Chemistry and Biology," *Critical Reviews in Oral Biology & Medicine* 13, no. 2 (2002): 155–170, https://doi.org/10.1177/154411130201300206.

16. X. Guo, L. Lei, H. Xiao, and J. Zheng, "Effect of Remineralisation on the Mechanical Properties and Tribological Behaviour of Human Tooth Dentine," *Biosurface and Biotribology* 6, no. 3 (2020): 92–95, https://doi.org/10.1049/bsbt.2020.0013.

17. Q. Yang, F. Li, Y. Ye, and X. Zhang, "Antimicrobial, Remineralization, and Infiltration: Advanced Strategies for Interrupting Dental Caries," *Medical Review* 5, no. 2 (2025): 87–116, https://doi.org/10.1515/mr-2024-0035.

18. World Health Organization, "Global Oral Health Status Report: Towards Universal Health Coverage for Oral Health by 2030," (2022), https://www.who.int/team/noncommunicable-diseases/global-status-report-on-oral-health-2022.ISBN978-92-4-006156-9.

19. E. Fleming and J. Afful, "Prevalence of Total and Untreated Dental Caries Among Youth: United States, 2015–2016," *NCHS Data Brief*, no. 307 (2018), https://stacks.cdc.gov/view/cdc/255767.

20. J. C. Carvalho and U. Schiffner, "Dental Caries in European Adults and Senior Citizens 1996–2016: ORCA Saturday Afternoon Symposium in Greifswald, Germany–part II," *Caries Research* 53, no. 3 (2019): 242–252, https://doi.org/10.1159/000492676.

21. H. Li, X. Wen, S. Li, et al., "Oral Health Conditions and Unmet Need Among Chinese Male Adults: A National Oral Health Survey," *BMC Public Health* 25, no. 1 (2025): 836, https://doi.org/10.1186/s12889-025-22070-2.

22. World Health Organization, "Oral Health Country Profile: Russian Federation," (2022), https://www.who.int/publications/m/item/oral-health-rus-2022-country-profile.

23. Y. Huang, Y. Wei, L. Zhang, et al., "Thin Film Morphology and Tribology Study in a Compliant Contact," *Biosurface and Biotribology* 11, no. 1 (2025): e70014, https://doi.org/10.1049/bsb2.70014.

24. V. B. Zelentsov, E. V. Sadyrin, A. G. Sukiyazov, and N. Y. Shubchinskaya, "On a Method for Determination of Poisson's Ratio and Young Modulus of a Material," *MATEC Web of Conferences* 226 (2018): 03027, https://doi.org/10.1051/matecconf/201822603027.

25. L. I. Krenev, S. S. Volkov, E. V. Sadyrin, T. I. Zubar', and S. A. Chizhik, "Mechanical Material Tests by the Nanoindentation Method at Various Indenter and Specimen Temperatures," *Journal of Engineering Physics and Thermophysics* 91, no. 3 (2018): 594–600, https://doi.org/10.1007/s10891-018-1780-5.

26. V. E. Burlakova, A. I. Tyurin, E. G. Drogan, et al., "Mechanical Properties and Size Effects of Self-Organized Film," *Journal of Tribology* 141, no. 5 (2019): 051601, https://doi.org/10.1115/1.4042678.

27. C. Yang, Y. Xiong, J. Wang, Y. Li, and W. Jiang, "Mechanical Characterization of Shale Matrix Minerals Using Phase-Positioned Nanoindentation and Nano-Dynamic Mechanical Analysis," *International Journal of Coal Geology* 229 (2020): 103571, https://doi.org/10.1016/j.coal.2020.103571.

28. L. Angk and M. V. Swain, "Nanoindentation: Application to Dental Hard Tissue Investigations," *Journal of Materials Research* 21, no. 8 (2006): 1893–1905, https://doi.org/10.1557/jmr.2006.0257.

29. L.-H. He and M. V. Swain, *Handbook of Nanoindentation: With Biological Applications* (CRC Press, 2019), 239–279.

30. E. V. Sadyrin, "Nanoindentation as a Tool for Characterizing Mechanical Properties of Dental Hard Tissues: Main Research Areas," *Mechanics of Solids* 60, no. 7 (2006): 5479–5492, https://doi.org/10.1134/S0025654425604537.

31. F. Lippert, D. M. Parker, and K. D. Jandt, "In Vitro Demineralization/Remineralization Cycles at Human Tooth Enamel Surfaces Investigated by AFM and Nanoindentation," *Journal of Colloid and Interface Science* 280, no. 2 (2004): 442–448, https://doi.org/10.1016/j.jcis.2004.08.016.

32. M. Finke, J. A. Hughes, D. M. Parker, and K. D. Jandt, "Mechanical Properties of in Situ Demineralised Human Enamel Measured by AFM Nanoindentation," *Surface Science* 491, no. 3 (2001): 456–467, https://doi.org/10.1016/S0039-6028(01)01311-5.

33. L. Angker, M. V. Swain, and N. Kilpatrick, "Characterising the Micro-Mechanical Behaviour of the Carious Dentine of Primary Teeth Using Nano-Indentation," *Journal of Biomechanics* 38, no. 7 (2005): 1535–1542, https://doi.org/10.1016/j.jbiomech.2004.07.012.

34. E. V. Sadyrin, "Correlating the Mechanical Properties to the Mineral Density of Brown Spot Lesion in Dentine Using Nanoindentation and X-Ray Micro-Tomography," *Advanced Materials Modelling for Mechanical. Medical and Biological Applications* (2021): 389–398, https://doi.org/10.1007/978-3-030-81705-3_21.

35. A. C. Fischer-Cripps, "Critical Review of Analysis and Interpretation of Nanoindentation Test Data," *Surface and Coatings Technology* 200, no. 14–15 (2006): 4153–4165, https://doi.org/10.1016/j.surfcoat.2005.03.018.

36. L. Shen, F. B. de Sousa, N. Tay, et al., "Deformation Behavior of Normal Human Enamel: A Study by Nanoindentation," *Journal of the Mechanical Behavior of Biomedical Materials* 108 (2020): 103799, https://doi.org/10.1016/j.jmbbm.2020.103799.

37. A. Chaiwat, N. Thirasupa, and O. Ajcharanukul, "Use of Micro-Computed Tomography and Scanning Electron Microscopy With Energy-Dispersive Spectroscopy to Distinguish Natural White Spot Enamel Lesions From Sound Enamel in Human Premolars," *Journal of Oral Science* 66, no. 1 (2024): 50–54, https://doi.org/10.2334/josnusd.23-0264.

38. S. R. G. Olivan, A. M. Deana, M. M. Pinto, et al., "Diagnosis of Occlusal Caries Lesions in Deciduous Molars by Coherent Light Scattering Pattern Speckle," *Photodiagnosis and Photodynamic Therapy* 18 (2017): 221–225, https://doi.org/10.1016/j.pdpdt.2017.03.004.

39. N. Arif, D. Beighton, and E. C. Sheehy, "Microbiological Assessment of Occlusal Brown-Spot Lesions in Primary Molars," *Caries Research* 40, no. 5 (2006): 398–402, https://doi.org/10.1159/000094285.

40. T. T. Y. Huang, L. H. He, M. A. Darendeliler, and M. V. Swain, "Nano-Indentation Characterisation of Natural Carious White Spot Lesions," *Caries Research* 44, no. 2 (2010): 101–107, https://doi.org/10.1159/000286214.

41. D. T. Yucesoy, H. Fong, C. Gresswell, et al., "Early Caries in an in Vivo Model: Structural and Nanomechanical Characterization," *Journal of Dental Research* 97, no. 13 (2018): 1452–1459, https://doi.org/10.1177/0022034518789898.

42. G. J. Joves, G. Inoue, A. Sadr, T. Nikaido, and J. Tagami, "Nano-indentation Hardness of Intertubular Dentin in Sound, Demineralized and Natural Caries-Affected Dentin," *Journal of the Mechanical Behavior of Biomedical Materials* 32 (2014): 39–45, https://doi.org/10.1016/j.jmbbm.2013.12.017.

43. G. J. Joves, G. Inoue, S. Nakashima, A. Sadr, T. Nikaido, and J. Tagami, "Mineral Density, Morphology and Bond Strength of Natural Versus Artificial Caries-Affected Dentin," *Dental Materials Journal* 32, no. 1 (2013): 138–143, https://doi.org/10.4012/dmj.2012-243.

44. B. R. Masters, "Abbe's Theory of Image Formation in the Microscope," *Superresolution Optical Microscopy* (2020): 65–108, https://doi.org/10.1007/978-3-030-21691-7_6.

45. W. C. Oliver and G. M. Pharr, "An Improved Technique for Determining Hardness and Elastic Modulus Using Load and Displacement Sensing Indentation Experiments," *Journal of Materials Research* 7, no. 6 (1992): 1564–1583, https://doi.org/10.1557/JMR.1992.1564.

46. W. C. Oliver and G. M. Pharr, "Measurement of Hardness and Elastic Modulus by Instrumented Indentation: Advances in Understanding and Refinements to Methodology," *Journal of Materials Research* 19, no. 1 (2004): 3–20, https://doi.org/10.1557/jmr.2004.19.1.3.

47. R. B. King, "Elastic Analysis of Some Punch Problems for a Layered Medium," *International Journal of Solids and Structures* 23, no. 12 (1987): 1657–1664, https://doi.org/10.1016/0020-7683(87)90116-8.

48. K. V. Gogolinskii, K. L. Gubskii, A. P. Kuznetsov, et al., "Investigation of the Metrological Characteristics of a Scanning Probe Measuring Microscope Using TGZ Type Calibration Gratings," *Measurement Techniques* 55, no. 4 (2012): 400–405, https://doi.org/10.1007/s11018-012-9972-4.

49. E. V. Sadyrin, "Modeling the Mechanism of Reducing Enamel Mineral Density in the Vicinity of the Fisure Tip," *Russian Journal of Biomechanics* 27, no. 1 (2023): 31–39, https://doi.org/10.15593/RJBiomech/2023.1.03.

50. V. B. Zelentsov, E. V. Sadyrin, B. I. Mitrin, and M. V. Swain, "Mathematical Tools for Recovery of the Load on the Fissure According to the Micro-CT Results," *Journal of the Mechanical Behavior of Biomedical Materials* 138 (2023): 105625, https://doi.org/10.1016/j.jmbbm.2022.105625.

51. B. Wan, M. Shahmoradi, Z. Zhang, et al., "Modelling of Stress Distribution and Fracture in Dental Occlusal Fissures," *Scientific Reports* 9, no. 1 (2019): 4682, https://doi.org/10.1038/s41598-019-41304-z.

52. P. Lagouvardos, P. Sourai, and G. Douvitsas, "Coronal Fractures in Posterior Teeth," *Operative Dentistry* 14, no. 1 (1989): 28–32.

53. I. R. Spears and R. H. Crompton, "The Mechanical Significance of the Occlusal Geometry of Great Ape Molars in Food Breakdown," *Journal of Human Evolution* 31, no. 6 (1996): 517–535, https://doi.org/10.1006/jhev.1996.0077.

54. P. Magne and U. C. Belser, "Porcelain Versus Composite Inlays/Onlays: Effects of Mechanical Loads on Stress Distribution, Adhesion, and Crown Flexure," *International Journal of Periodontics and Restorative Dentistry* 23, no. 6 (2003): 543–555.

55. P. Bourdiol and L. Mioche, "Correlations Between Functional and Occlusal Tooth-Surface Areas and Food Texture During Natural Chewing Sequences in Humans," *Archives of Oral Biology* 45, no. 8 (2000): 691–699, https://doi.org/10.1016/S0003-9969(00)00027-3.

56. S. G. Salis, J. A. Hood, A. N. Stokes, and E. E. Kirk, "Patterns of Indirect Fracture in Intact and Restored Human Premolar Teeth," *Dental Traumatology* 3, no. 1 (1987): 10–14, https://doi.org/10.1111/j.1600-9657.1987.tb00165.x.

57. N. Murakami and N. Wakabayashi, "Finite Element Contact Analysis as a Critical Technique in Dental Biomechanics: A Review," *Journal of Prosthodontic Research* 58, no. 2 (2014): 92–101, https://doi.org/10.1016/j.jpor.2014.03.001.

58. M. Shahmoradi, B. Wan, Z. Zhang, M. Swain, and Q. Li, "Mechanical Failure of Posterior Teeth due to Caries and Occlusal wear-A Modelling Study," *Journal of the Mechanical Behavior of Biomedical Materials* 125 (2022): 104942, https://doi.org/10.1016/j.jmbbm.2021.104942.

59. C. D. Lynch and R. J. McConnell, "The Cracked Tooth Syndrome," *Journal of the Canadian Dental Association* 68, no. 8 (2002): 470–475.

60. S. Banerji, S. B. Mehta, and B. J. Millar, "Cracked Tooth Syndrome. Part 1: Aetiology and Diagnosis," *British Dental Journal* 208, no. 10 (2010): 459–463, https://doi.org/10.1038/sj.bdj.2010.449.

61. L. Pang, Y. Wang, Y. Ye, Y. Zhou, Q. Zhi, and H. Lin, "Metagenomic Analysis of Dental Plaque on Pit and Fissure Sites With and Without Caries Among Adolescents," *Frontiers in Cellular and Infection Microbiology* 11 (2021): 740981, https://doi.org/10.3389/fcimb.2021.740981.

62. N. M. Leal, J. L. Silva, M. I. M. Benigno, E. A. Bemerguy, J. B. Meira, and R. Y. Ballester, "How Mechanical Stresses Modulate Enamel Demineralization in Non-Carious Cervical Lesions?," *Journal of the Mechanical Behavior of Biomedical Materials* 66 (2017): 50–57, https://doi.org/10.1016/j.jmbbm.2016.11.003.

63. P. Senna, A. Del Bel Cury, and C. Rösing, "Non-Carious Cervical Lesions and Occlusion: A Systematic Review of Clinical Studies," *Journal of Oral Rehabilitation* 39, no. 6 (2012): 450–462, https://doi.org/10.1111/j.1365-2842.2012.02290.x.

64. E. Sadyrin, M. Swain, B. Mitrin, et al., "Characterization of Enamel and Dentine About a White Spot Lesion: Mechanical Properties, Mineral Density, Microstructure and Molecular Composition," *Nanomaterials* 10, no. 9 (2020): 1889, https://doi.org/10.3390/nano10091889.

65. M. Shahmoradi and M. V. Swain, "Micro-CT Analysis of Naturally Arrested Brown Spot Enamel Lesions," *Journal of Dentistry* 56 (2017): 105–111, https://doi.org/10.1016/j.jdent.2016.11.007.

66. Y. Kitasako, A. Sadr, Y. Shimada, M. Ikeda, Y. Sumi, and J. Tagami, "Remineralization Capacity of Carious and Non-Carious White Spot Lesions: Clinical Evaluation Using ICDAS and SS-OCT," *Clinical Oral Investigations* 23, no. 2 (2019): 863–872, https://doi.org/10.1007/s00784-018-2503-1.

67. J. Palamara, P. P. Phakey, W. A. Rachinger, and H. J. Orams, "Ultrastructure of the Intact Surface Zone of White Spot and Brown Spot Carious Lesions in Human Enamel," *Journal of Oral Pathology & Medicine* 15, no. 1 (1986): 28–35, https://doi.org/10.1111/j.1600-0714.1986.tb00560.x.

68. S. Stoleriu, G. Iovan, G. Pancu, A. Georgescu, A. Moldovanu, and S. Andrian, "Study on the Effects of Acid Etching on Affected Enamel," *International Journal of Medical Dentistry* 13, no. 4 (2011): 253–257.

69. A. Boyde and D. Mills, "Enamel Tubules and Spindles: Enter and Exit the Amelocyte," *Calcified Tissue International* 117, no. 1 (2026): 81, https://doi.org/10.1007/s00223-026-01522-w.

70. S. Siddiqui, P. Anderson, and M. Al-Jawad, "Recovery of Crystallographic Texture in Remineralized Dental Enamel," *PLoS One* 9, no. 10 (2014): e108879, https://doi.org/10.1371/journal.pone.0108879.

71. C. Robinson, R. C. Shore, S. J. Brookes, S. Strafford, S. R. Wood, and J. Kirkham, "The Chemistry of Enamel Caries," *Critical Reviews in Oral Biology & Medicine* 11, no. 4 (2000): 481–495, https://doi.org/10.1177/10454411000110040601.

72. L. M. Silverstone and M. J. Hicks, "The Structure and Ultrastructure of the Carious Lesion in Human Dentin," *Gerodontics* 1, no. 4 (1985): 185–193, PMID: 3864713.

73. I. M. Gheorghiu, S. Ciobanu, I. Roman, S. Păunică, A. S. Dumitriu, and A. A. Iliescu, "Deep Caries Lesions Revisited: A Narrative Review," *Journal of Mind and Medical Sciences* 12, no. 1 (2025): 37, https://doi.org/10.3390/jmms12010037.

74. G. Daculsi, R. Z. LeGeros, A. Jean, and B. Kerebel, "Possible Physico-Chemical Processes in Human Dentin Caries," *Journal of Dental Research* 66, no. 8 (1987): 1356–1359, https://doi.org/10.1177/00220345870660081401.

75. L. E. Bertassoni, S. Habelitz, J. H. Kinney, S. J. Marshall, and G. W. Marshall Jr, "Biomechanical Perspective on the Remineralization of Dentin," *Caries Research* 43, no. 1 (2009): 70–77, https://doi.org/10.1159/000201593.

76. J. M. Ten Cate, "Remineralization of Caries Lesions Extending Into Dentin," *Journal of Dental Research* 80, no. 5 (2001): 1407–1411, https://doi.org/10.1177/00220345010800050401.

77. M. Maltz, E. F. de Oliveira, V. Fontanella, and R. Bianchi, "A Clinical, Microbiologic, and Radiographic Study of Deep Caries Lesions After Incomplete Caries Removal," *Quintessence International* 33, no. 2 (2002).

78. M. K. Arifa, R. Ephraim, and T. Rajamani, "Recent Advances in Dental Hard Tissue Remineralization: A Review of Literature," *International journal of Clinical Pediatric Dentistry* 12, no. 2 (2019): 139–144, https://doi.org/10.5005/jp-journals-10005-1603.

79. F. R. Tay and D. H. Pashley, "Guided Tissue Remineralisation of Partially Demineralised Human Dentine," *Biomaterials* 29, no. 8 (2008): 1127–1137, https://doi.org/10.1016/j.biomaterials.2007.11.001.

80. J. M. Ten Cate and J. D. B. Featherstone, "Mechanistic Aspects of the Interactions Between Fluoride and Dental Enamel," *Critical Reviews in Oral Biology & Medicine* 2, no. 3 (1991): 283–296, https://doi.org/10.1177/10454411910020030101.

81. J. M. Ten Cate, "Remineralization of Deep Enamel Dentine Caries Lesions," *Australian Dental Journal* 53, no. 3 (2008): 281–285, https://doi.org/10.1111/j.1834-7819.2008.00063.x.

82. D. Tantbirojn, R. J. Feigal, and A. Versluis, "Remineralized Dentin Lesions Induced by Glass Ionomer Demonstrate Increased Resistance to Subsequent Acid Challenge," *Quintessence International* 37, no. 4 (2006).

83. A. Kishen and S. Vedantam, "Hydromechanics in Dentine: Role of Dentinal Tubules and Hydrostatic Pressure on Mechanical Stress–Strain Distribution," *Dental Materials* 23, no. 10 (2007): 1296–1306, https://doi.org/10.1016/j.dental.2006.11.018.

84. J. C. Hay and G. M. Pharr, "Critical Issues in Measuring the Mechanical Properties of Hard Films on Soft Substrates by Nanoindentation Techniques," *MRS Online Proceedings Library* 505 (1997): 65, https://doi.org/10.1557/PROC-505-65.

85. E. V. Sadyrin, A. L. Nikolaev, A. S. Vasiliev, and I. Yu. Golushko, "Nanoindentation Derived Mechanical Properties of Au Thin Film Deposited by Pulsed Laser Sputtering on Si Substrate," *International Conference on Physics and Mechanics of New Materials and Their Applications* 10 (2021): 215–222, https://doi.org/10.1007/978-3-030-76481-4_19.

86. I. Yu. Golovin, Nanoindentation and Its Capabilities. [in Russian], (2009).312

87. L. H. He and M. V. Swain, "Nanoindentation Creep Behavior of Human Enamel," *Journal of Biomedical Materials Research Part A* 91, no. 2 (2009): 352–359, https://doi.org/10.1002/jbm.a.32223.

88. Z. H. Xie, E. K. Mahoney, N. M. Kilpatrick, M. V. Swain, and M. Hoffman, "On the Structure–Property Relationship of Sound and Hypomineralized Enamel," *Acta Biomaterialia* 3, no. 6 (2007): 865–872, https://doi.org/10.1016/j.actbio.2007.05.007.

89. Z. Xie, M. V. Swain, and M. J. Hoffman, "Structural Integrity of Enamel: Experimental and Modeling," *Journal of Dental Research* 88, no. 6 (2009): 529–533, https://doi.org/10.1177/0022034509337130.

90. J. T. Varghese, B. Babaei, P. Farrar, L. Prentice, and B. G. Prusty, "Influence of Thermal and Thermomechanical Stimuli on a Molar Tooth Treated With Resin-Based Restorative Dental Composites," *Dental Materials* 38, no. 5 (2022): 811–823, https://doi.org/10.1016/j.dental.2022.04.010.

91. M. Del Fabbro, S. Khijmatgar, B. Vandenberghe, et al., "Oral Health of Astronauts in Short-and Long-Term Missions in Space," *Aerospace Medicine and Human Performance* 96, no. 2 (2025): 168–179, https://doi.org/10.3357/AMHP.6372.2025.

92. E. V. Sadyrin, D. V. Yogina, S. S. Volkov, and S. M. Aizikovich, "Evaluation of Density and Microgeometrical Characteristics of glass-ionomer Cement and Composite Resin Fillings: A Biomechanical Ex Vivo Study," *Russian Journal of Biomechanics* 26, no. 2 (2022): 67–73, https://doi.org/10.15593/RJBiomech/2022.2.06.

93. R. E. Gonzalez-Valenzuela, Q. T. Vu, P. Mettes, B. G. Loos, H. Marquering, and E. Berkhout, "Microtomography to Traditional Dental Radiograph: Projecting 3-Dimensional Initial Proximal Caries Lesion Annotations for Enhanced Radiographic Delineation," *Dentomaxillofacial Radiology* 54, no. 4 (2025): 320–328, https://doi.org/10.1093/dmfr/twae058.

94. L. Zhang, L. Liu, X. Li, Y. Tang, C. Liu, and H. P. Zhang, "Interactions Between Stearic Acid and Calcite Surfaces: Experimental and Computer Simulation Studies," *Biosurface and Biotribology* 7, no. 3 (2021): 126–132, https://doi.org/10.1049/bsb2.12017.

95. A. Butera, M. Pascadopoli, S. Gallo, et al., "SEM/EDS Evaluation of the Mineral Deposition on a Polymeric Composite Resin of a Toothpaste Containing Biomimetic Zn-Carbonate Hydroxyapatite (microRepair®) in Oral Environment: A Randomized Clinical Trial," *Polymers* 13, no. 16 (2021): 2740, https://doi.org/10.3390/polym13162740.

96. J. A. Arsecularatne, N. R. Chung, and M. Hoffman, "An in Vitro Study of the Wear Behaviour of Dental Composites," *Biosurface and Biotribology* 2, no. 3 (2016): 102–113, https://doi.org/10.1016/j.bsbt.2016.09.002.

97. I. Otel, "Overall Review on Recent Applications of Raman Spectroscopy Technique in Dentistry," *Quantum Beam Science* 7, no. 1 (2023): 5, https://doi.org/10.3390/qubs7010005.

98. P. S. Ungar and A. T. Hara, "On the Use of Dental Microwear Texture Analysis to Determine Aetiology and Assess Wear of Dental Tissues for Clinical Evaluation," *Biosurface and Biotribology* 11, no. 1 (2025): e12089, https://doi.org/10.1049/bsb2.12089.

99. E. Y. O. Balaev, "On Self-Positioning and Self-Fixation of Parts Made of Alloys With Shape Memory Effect Under Component Assembling," *Advanced Engineering Research (Rostov-on-Don)* 24, no. 3 (2024): 238–245, https://doi.org/10.23947/2687-1653-2024-24-3-238-245.

100. E. Sajewicz and S. Wojda, "Tribological Interactions Between Tooth Enamel and Composite Dental Materials," *Biosurface and Biotribology* 3, no. 4 (2017): 144–154, https://doi.org/10.1016/j.bsbt.2017.12.007.

101. Y. Luo, L. Yang, C. Liu, L. Yan, and C. Xie, "Functional Hydrogels for the Treatment of Periodontitis," *Biosurface and Biotribology* 11, no. 1 (2025): e70009, https://doi.org/10.1049/bsb2.70009.

102. K. V. Gubareva and A. V. Eremin, "Numerical Solution to the Problem of Thermal Conductivity in a Porous Plate With a Topology of Triply Periodic Minimal Surfaces," *Advanced Engineering Research (Rostov-on-Don)* 25, no. 1 (2025): 23–31, https://doi.org/10.23947/2687-1653-2025-25-1-23-31.

103. T. J. Ko, K. M. Byrd, and S. A. Kim, "The Chairside Periodontal Diagnostic Toolkit: Past, Present, and Future," *Diagnostics* 11, no. 6 (2021): 932, https://doi.org/10.3390/diagnostics11060932.

104. I. N. Sneddon, "The Relation Between Load and Penetration in the Axisymmetric Boussinesq Problem for a Punch of Arbitrary Profile," *International Journal of Engineering Science* 3, no. 1 (1965): 47–57, https://doi.org/10.1016/0020-7225(65)90019-4.

Appendix A: Calculation of Mechanical Properties via Nanoindentation

Throughout the experiment, the indenter displacement h was continuously monitored as the load P was applied. The peak displacement reached at the maximum load P_{max} was identified as h_{max}. Consequently, each test resulted in a characteristic load–displacement curve. Holding load at its maximum value for a time before unloading eliminated the effect of the creep response on the unloading 'branch'. The unloading portion of the curve was then fitted using the following function:

$$P = a(h - h_r)^m, \tag{A1}$$

where a and m represent the fitting parameters, and h_r is the residual depth of the imprint, that is, the amount of the displacement remaining once the material no longer exerts a resistive force during unloading. Using this approximation, the derivative called indentation stiffness S was determined at h_{max}:

$$S = \frac{dP}{dh}, \tag{A2}$$

To evaluate the reduced Young's modulus the following formula was used:

$$E_r = \frac{S\sqrt{\pi}}{2\beta\sqrt{A_c}}, \tag{A3}$$

where A_c is the projected contact area (the projection of the contact surface on a plane orthogonal to the axis of indentation), β is a correction factor. Subsequently, the indentation hardness was determined via the following relation:

$$H = \frac{P_{max}}{A_c}. \tag{A4}$$

The contact depth h_c represents the depth along which the Berkovich indenter maintains physical contact with the tooth tissue (enamel or dentine) at the peak load, excluding the deflection of the surrounding surface. For its determination the following algorithm was used:

— We calculated h_s representing the depth of surface deflection outside of contact

$$h_s = \epsilon\frac{P_{max}}{S}, \tag{A5}$$

where ϵ represents a geometric factor determined by the shape of the indenter tip; given that unloading behaviours are most

accurately modelled by assuming an indenter geometry analogous to a paraboloid of revolution, a standard value of $\epsilon = 0.75$ was established [104] and remains the conventional benchmark for nanoindentation data processing [46];

— The contact depth was calculated as

$$h_c = h_{max} - h_s, \tag{A6}$$

where h_{max} is determined by the nanoindentation system.

Appendix B: Supplementary Experimental Data

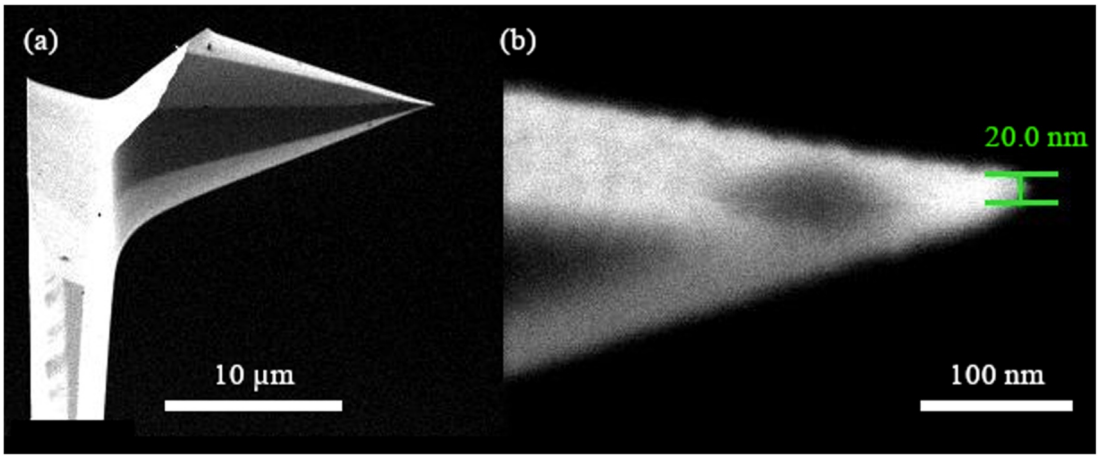

FIGURE B1 | SEM characterisation of the AFM probe tip condition: (a) low-magnification view of the cantilever, accelerating voltage 1.5 kV; (b) high-magnification close-up of the sharp probe tip, accelerating voltage 2 kV.

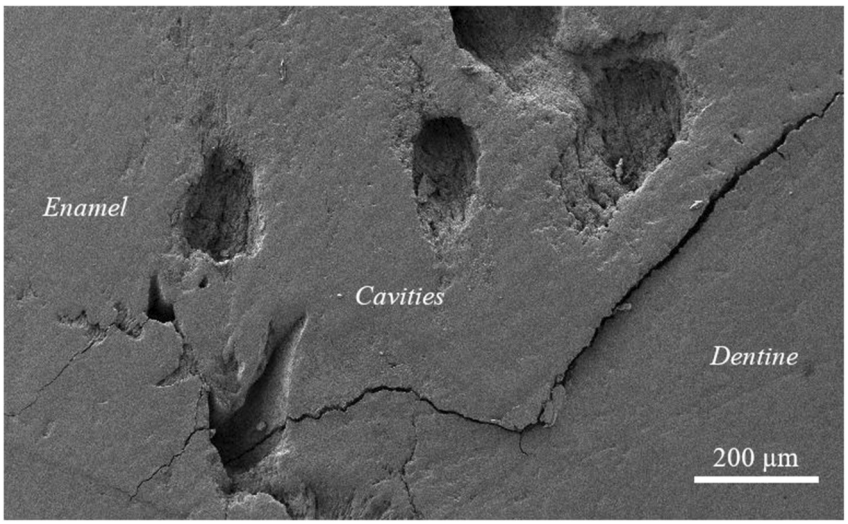

FIGURE B2 | SEM micrograph of DEJ, Sample 2, Section 3.